March 2017

Deformation and Adhesion of Soft Composite Systems for Bio-inspired Adhesives and Wrinkled Surface Fabrication

Michael Imburgia

DEFORMATION AND ADHESION OF SOFT COMPOSITE SYSTEMS FOR BIO-INSPIRED ADHESIVES AND WRINKLED SURFACE FABRICATION

A Dissertation Presented

by

MICHAEL JAMES IMBURGIA

Submitted to the Graduate School of the
University of Massachusetts Amherst in partial fulfillment
of the requirements for the degree of

DOCTOR OF PHILOSOPHY

February 2017

Polymer Science and Engineering

DEFORMATION AND ADHESION OF SOFT COMPOSITE SYSTEMS FOR BIO-INSPIRED ADHESIVES AND WRINKLED SURFACE FABRICATION

A Dissertation Presented

by

MICHAEL JAMES IMBURGIA

Approved as to style and content by:

Alfred J. Crosby, Chair

Alan J. Lesser, Member

Ian R. Grosse, Member

Duncan J. Irschick, Member

E. Bryan Coughlin, Department Chair
Polymer Science and Engineering

DEDICATION

To Mom, Dad, Anthony, and Justin.

ACKNOWLEDGMENTS

When I was an undergraduate contemplating what to do after I graduated, I had several advisors along the way, to whom I asked: "Do you know any good programs or professors of materials science that would take a mechanical engineer?" Four separate people told me to look up Al Crosby at UMass. So I did. I visited the group website and saw a picture of a decently handsome guy with dark hair and a big smile - and also some interesting images of research on the snapping mechanism of the Venus Flytrap. A while later, I arrived on UMass campus to visit and met Al, a warm and welcoming guy with *silvery-grey* hair. Though I was slightly betrayed by his appearance, I still came away with an awesome first impression. Even after five years of advising me, Al is just as warm and welcoming. Along the way he has made my PhD experience more like an apprenticeship and less like a stressful job; he has led by example, invested his valuable time to guide me through research, answered simple questions I should have known from reading the literature, and motivated me when my results were not what I had expected. I am truly grateful for being at the receiving end of such great mentoring. Thanks Al!

To my committee members, Professor Alan Lesser, Professor Ian Grosse, and Professor Duncan Irschick - thank you for your time, intellectual insight, and professional input into my research and presenting skills. I put together a committee that I hoped would help me defend my PhD work, but you all helped me build skills to advocate for my research; instructing me how to "sell" my projects and how to convincingly argue minute points. These skills are invaluable to my future, thank you.

To the Crosby Group members past and present with whom I have spent countless hours with, Dong Yun, Chelsea, Hyun Suk, Sammy P, Mike B., Yuri, Jun, Cheol,

Shelby, Sami, Jon, Dan, Marcos, UJ, Yu-Cheng, Minchao, Shruti, Satyan, Richard, Chya-Yan, Yongjin, David, Kasey, Konane, Dylan, Chris, Mark, Martin, and Christian - thank you for all of your help inside and outside of lab, at conferences, at cookouts, and in the offices. You will always be a part of my academic family and if you need *anything* you know I will give too much of my time to try to help you out. To Hannah and Brian, my research hands, you have taught me so much about how to be a better mentor, even if it was at your expense. To Mike B., Dan, Satyan, and Chris, thanks for your input and help with Geckskin® and adhesion related projects. Thanks especially to Mike B. and Dan for doing the leg work to make me a TV star. To Hyun Suk, Yuri, Marcos, and Yu-Cheng, thanks for getting me pumped to wrinkle. To Sami, Jon, and Shruti, thanks for being outstanding office mates, enduring my singing and tolerating the look of my disheveled desk. And to Minchao, my academic twin, your unexpected sarcastic comments are a breath of fresh air much needed when confined to research for too long. I cannot wait to see where your career will take you next.

To the PSE community in Conte, including the Class of 2011, Nakul, Joel, Connor, Sveta, Madhura, Daniel, Piril, Gajin, Jaewon, Zhiwei, Pat, Alex, Alper, Jana, and Minchao, and all of my "Entropic Thunder" teammates, we all kept each other entertained and focused on life outside of Conte and I am so grateful. To my roommates Joel, Nakul, and Nihal, there are too many good meals, parties, barbecues, river floats, salsa dances, potato bugs, hikes, and moments to mention, but I hope you three know how enjoyable you made this PhD.

To my biology collaborators, Duncan and Casey - thanks for educating me on biology and the importance of statistics in science. I have enjoyed working with you both and GV3 (my favorite gecko) and look forward to collaborating in the future. To Andy, I have enjoyed our numerous sessions of Instron testing, mainly for me asking ridiculous questions about the Brits. To my Cambridge colleagues from the Glover

and Federle research groups, especially Beverley, Walter, Edwige, Aleks, and David - thanks for welcoming me into your groups and teaching me about the complexities of plant biology and insect zoology. It was only five weeks but it helped broaden my research, cultural, and eating perspectives immensely.

To my friends from Binghamton and Oyster Bay, Jimmy, Kirstie, Greg Frag, Dave, Chris, Greg Kuester, B-face, Putt, Nakrin, Collery, and Demaria - thanks for staying in touch and pretending to be amazed when I talk about my research. To my extended family, Uncle Tony, Aunt Nancy, Anthony, Matt, Richie, Kim, Jake, Ben, Billy, Uncle Ray, Sue, John, Lisa, Jon, Uncle Tom, Aunt Bonnie, Todd, Michelle, Toni, and Matt - thank you for supporting me during my PhD work via barbecues and family reunions. To Uncle Tony especially, you are the one who taught me to be curious, starting with memorizing the capitals of the United States in 2nd grade. A PhD cannot be had without a healthy dose of curiosity - thank you.

To my other family, Bob, Ann-Delia, Sarah, and Katrina - thanks for asking tons of questions I did not know the answer to and for making the latter portion of my PhD work more enjoyable than I thought it would be. To my favorite roommate Katrina, thank you for making sure I was fed, clothed, and bathed while writing my thesis. I lost track of time while in the writing/figure making zone and you provided unconditional support to make it happen. Also, there is no doubt this thesis would have taken another year or so to complete if it were not for your "encouragement":

"Did you write your prospectus yet?"

"Did you write your IRP yet?"

"Did you finish preparing your data defense yet?"

"Are you looking for jobs yet?"

Thanks for providing the tough love I needed. I love you.

And to my family, my brother Justin, my brother Anthony, my dad Joe, and my mom Fran - all of my work during undergraduate school and graduate school

was motivated by you. I know we are not a family that shows a lot of love, but we are definitely a family that knows a lot of love. To Justin and Anthony, thanks for teaching me how not to be a nerd and for showing me how to listen to, play, and sing all kinds of music - an invaluable resource when frustrated with graduate school. To Dad, for knowing more about my research than anyone outside of Amherst and for teaching me patience, which is critical when science is not on your side. And to Mom, thanks for showing me real strength and teaching me that complaining would get me nowhere, a skill and advice that definitely came in handy more than once during my time in graduate school. Mom, wherever you are, I hope you get to read this dissertation that I absolutely, never uttered a single complaint about. I love you all.

Dan King: "Al, I think we have the best research group in PSE."

Al Crosby: "Yeah man. Who's got tulips like these?"

ABSTRACT

DEFORMATION AND ADHESION OF SOFT COMPOSITE SYSTEMS FOR BIO-INSPIRED ADHESIVES AND WRINKLED SURFACE FABRICATION

FEBRUARY 2017

MICHAEL JAMES IMBURGIA

B.S., STATE UNIVERSITY OF NEW YORK AT BINGHAMTON

M.S., UNIVERSITY OF MASSACHUSETTS AMHERST

Ph.D., UNIVERSITY OF MASSACHUSETTS AMHERST

Directed by: Professor Alfred J. Crosby

The study of soft material deformation and adhesion has broad applicability to industries ranging from automobile tires to medical prosthetics and implants. When a mechanical load is imposed on a soft material system, a variety of issues can arise, including non-linear deformations at interfaces between soft and rigid components. The work presented in this dissertation embraces the occurrence of these non-linear deformations, leading to the design of functional systems that incorporate a soft elastomer layer with application to bio-inspired adhesives and wrinkled surface fabrication. Understanding the deformation of a soft elastomer layer and how the system loading and geometry influence non-linear mechanical transitions, including interfacial failure and surface buckling, are crucial for predicting the performance of the mechanical system. This dissertation focuses on three soft composite systems of particular interest: (1)

a multi-component, multiple adhesive contact surface device that allows for control of reversible adhesive force with geometric arrangement, (2) a confined isolated shear contact and an elastomeric coating, where the deformation and adhesion scale with the degree of confinement, and (3) a thin film lamination technique involving a soft substrate, where surface wrinkles are created and tuned in a continuous manner by controlling interfacial strains via applied contact load and substrate curvature.

We first study the deformation and adhesion of a multi-component fabric-elastomer system with multiple adhesive contacts, or "digits". We conduct lap adhesion experiments in a model three digit system, finding that increasing angular spacing between adhesive digits increases system compliance and attenuates adhesive force capacity. To describe these findings we develop several relationships between system loading, materials properties, and geometry. We develop an equation which describes the relationship of system compliance with individual digit compliance and angular spacing between adhesive digits that agrees well with experimental data. Additionally, we derive equations for adhesive force capacity in a multiple adhesive contact system that agree well with experimental data. These explicit equations not only relate angular spacing with force capacity, but include critical strain energy release rate, digit compliance, and contact area. The equations derived and verified in this study will lead to more complex adhesive device design, as well as provide a foundation for studying the biomechanics of animals that use adhesion for locomotion.

Next, we examine the deformation and adhesion of a rigid punch contacting and shearing a thin elastic coating. Using experiment we find that increasing confinement leads to a decrease in compliance and an increase in adhesive force capacity. We develop an explicit, semi-empirical equation with the help of finite element analysis to describe the influence of confinement ratio on shear compliance. This derived equation agrees with our experimental data, with the exception of a few data points that deviate due to a pronounced normal force component. Additionally, we derive an equation

for adhesive force capacity as a function of confinement, elastic coating modulus, and critical strain energy release rate. We find experimentally that an increase in adhesive force capacity was largely dictated by an increase in confinement, with some additional contributions attributed to dissipative processes confined to the adhesive crack tip. These equations will serve as a guide for decoupling the contributions of geometry and materials parameters to adhesive force in systems involving a thin elastic layer.

Lastly, we develop a fabrication technique that transforms the existing manufacturing process of film lamination to create tunable wrinkled surfaces in a thin film/soft elastomer composite. We conduct experiments to find that the process parameters of applied contact load and roller curvature can be used to control wrinkle aspect ratio. Our experimental results convey that increasing applied contact load and decreasing roller radius lead to an increase in wrinkle amplitude. Using both experimental results and finite element analysis, we develop a relation between wrinkle aspect ratio and the process parameters of applied contact load and roller curvature. This explicit equation allows us to predict the change in wrinkle amplitude for a given materials system as process parameters are tuned using our modified film lamination technique. Wrinkled surface technology has been envisioned in many applications ranging from optoelectronics to enhanced adhesives. The technique presented here to tune wrinkle size in a continuous process can lead to the large scale manufacturing of these previously proposed wrinkling technologies.

TABLE OF CONTENTS

LIST OF TABLES

Table **Page**

LIST OF FIGURES

Figure **Page**

CHAPTER 1

INTRODUCTION

1.1 Overview

Soft materials, such as elastomers, gels, and biological tissues, exhibit elastic behavior when subject to characteristically large strains. These materials are the basis of many emerging technologies including soft robotics [1, 2, 3], 3D printed biological materials [4, 5, 6], bio-inspired adhesives [7, 8, 9], and stretchable and flexible electronics [10, 11, 12]. Many of these technologies incorporate materials and structures of widely varied mechanical properties, forming physical interfaces that can be problematic for engineering design. When these soft composite systems undergo finite deformations, interfacial stresses arise due to a mismatch in materials properties, leading to non-linear mechanical transitions including material fracture, interfacial failure, and surface buckling. Understanding the development of interfacial stresses is critical for predicting the limits of mechanical performance within soft composite systems.

This dissertation begins with a brief overview of soft materials mechanics and the adhesion involved in maintaining contact between soft and rigid surfaces. Following introductory material, backgrounds on specific applications of bio-inspired adhesion and wrinkled surface fabrication are discussed. The main content of this dissertation is captured by the following questions, which serve as the intellectual merit of the work:

- *How does angular spacing influence the force capacity and compliance of a multi-component shear adhesive device?*

- *How does confinement affect the shear deformation and adhesion behavior of an isolated contact and a soft elastomer coating?*

- *How can the deformation of an elastomer during a thin film-elastomer lamination process lead to the fabrication of tunable surface structures?*

The scientific impact of this dissertation is two fold. First, it builds upon the foundation of reversible adhesion work to advance bio-inspired adhesive device design, to guide studies for performing quantitative biomechanical analyses for animals that use adhesion, and to incorporate the influence of system confinement on reversible adhesive performance. Secondly, this dissertation adds value to the existing multilayer composite manufacturing technique of film lamination by applying knowledge of rolling contact models and soft material/thin film composite characterization to tune controlled surface structures. With these findings, more complex manufacturing designs and device optimizations for soft composites systems can be achieved.

1.2 Polymer materials mechanics

The mechanics of materials encompasses the elastic response of materials to body or surface forces and the limits at which these materials undergo irreversible failure. When choosing a material for mechanical function, we often consider elastic properties such as material modulus, Poisson's ratio, and resilience. For designing and predicting material failure we might consider the fracture energy, the work of adhesion, or strain at break. This section will provide a broad overview of the materials mechanics relevant to the ensuing studies.

The stress-strain response of polymeric materials from a continuum mechanics perspective is often linear-elastic at a fixed temperature, fixed rate, and fixed pressure. The ratio of stress to strain during the initial mechanical response of a linear-elastic polymeric material, termed Young's modulus, is largely determined by the mobility

of the polymer backbone. The materials used throughout this dissertation are elastomers and rigid thermoplastic polymers. Elastomers are materials that are liquid-like and mobile on the molecular scale, but on the macroscopic scale, due to a percolating connection between molecules called cross-links, are elastic. This liquid-like behavior on the molecular scale gives elastomers their soft properties, seen in systems such as natural rubber and siloxanes. Rigid thermoplastic polymers are materials that are below their glass transition temperature, or the temperature below which the polymer backbone mobility is reduced, resulting in stiffer mechanical responses. Classes of rigid thermoplastic polymers include amorphous polymers, such as poly(styrene) and poly(carbonate), and semi-crystalline polymers, such as poly(amide 6,6). Although knowledge of rigid thermoplastic polymer deformation and failure are critical for understanding the limits of the highlighted systems that involve thin, rigid poly(styrene) films and rigid poly(amide 6,6) fabrics, the larger portion of materials mechanics in the studies presented here involve elastomer mechanics, so much of the focus will be on phenomena related to elastomers.

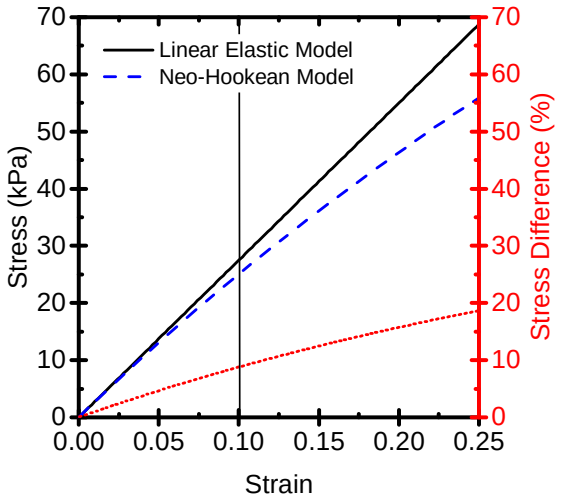

Figure 1.1. Linear-elastic and neo-Hookean constitutive behavior. Young's modulus of 275 kPa. Equation 1.1 is represented by the solid black line. Equation 1.2 is represented by the dashed blue line. The percent difference in stress between the two models as a function of strain is represented by the dotted red line. Values for the stress difference are indicated on the right axis.

In the low strain limit, i.e., $\varepsilon < 0.1$, the stress-strain response of elastomers can be approximated as linear-elastic. The constitutive relation for an isotropic, linear-elastic solid in uniaxial tension is represented by

$$\sigma_{eng} = E\varepsilon_{eng} \tag{1.1}$$

where σ_{eng} is the engineering stress in the extension direction, E is the Young's modulus, and ε_{eng} is the engineering strain in the extension direction. Though this model is a good approximation for elastomers at low strain, the experimentally observed behavior of elastomers at finite strains is characterized by a slope that changes with applied strain, known as a hyperelastic constitutive relation.

Hyperelastic models have been proposed previously, some of which are derived from entropic elasticity of polymer chains (e.g., neo Hookean model), and others that are developed via a phenomenological continuum mechanics approach (e.g., Mooney-Rivlin model) [13]. The constitutive relation for an isotropic, incompressible neo-Hookean solid in uniaxial tension is represented by

$$\sigma_{eng} = \frac{E}{3}\left(\lambda - \frac{1}{\lambda^2}\right) \tag{1.2}$$

where λ is the stretch ratio, defined as $1+\varepsilon_{eng}$. Figure 1.1 shows the deviation of a neo-Hookean constitutive model from a linear-elastic constitutive model at finite strains. In the ensuing studies, we subject our elastomers to average strains that do not exceed 0.1, justifying the use of linear-elastic constitutive relations for analytical equations. However, in some of the loading geometries and stress states presented, local strains may exceed 0.1. For finite element models that support experiments, we use neo-Hookean constitutive relations to better capture local stress states in elastomers. Beyond material modulus, the materials properties relevant to mechanical function that we consider include the work of adhesion between an elastomer and a contacting

surface. These materials properties will be addressed in the fundamentals of adhesion chapter.

1.3 Adhesion of soft materials

The fundamental study of soft material friction and adhesion has garnered widespread interest for its applicability to automobiles (e.g., tires and brake pads), the adhesives industry (e.g., tapes and sealants), biomedical devices (e.g., synthetic cartilage and skin applications), and even athletic performance (e.g., traction during running). Adhesion is defined as the force or collective forces that preserve contact between two individual bodies. Studying problems of adhesion requires an understanding of atomic interactions between the two surfaces, chemical compositions of the two surface materials, and elasticity of the contacting bodies. The adhesion presented throughout this dissertation involves the contact between two initially separated bodies, where the primary intermolecular forces are omnipresent van der Waals forces.

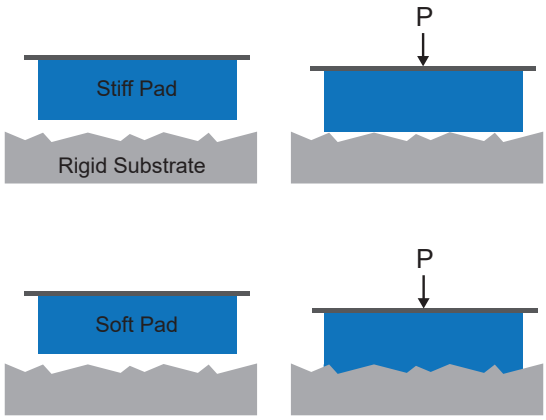

Figure 1.2. Soft material contact. A stiff pad of material pressed into contact with an arbitrarily rough surface by a load, P, results in very little real contact area. A softer pad pressed into contact with an arbitrarily rough surface by a load P results in greater contact area. If the load is removed, contact can remain for the soft pad as long as the adhesion energy between the soft pad and rough surface is greater than the energy required to deform the soft pad.

van der Waals forces are dispersive intermolecular interactions that occur between the molecules of any two surfaces and are especially prominent when two surfaces are within several nanometers [14]. In order to make such intimate contact and maximize total contact area, two bodies in close proximity must either have a low degree of surface roughness or a low stiffness such that an applied normal pressure can maximize contact. Figure 1.2 highlights this concept, where at a fixed normal load, more conformal contact is achieved when a material is soft enough to conform to surface asperities. However, once the normal load is removed, the maintenance of adhesive contact is dependent on the competition between elasticity of the substrate, surface roughness, and strength of van der Waals interactions between the two specific bodies. The following section presents an energy balance to describe the adhesive failure between two elastic bodies, incorporating contributions of van der Waals forces as well as material elasticity.

1.3.1 Adhesion energy balance

For two perfectly smooth, rigid surfaces in contact, under thermodynamic equilibrium, the energy required to separate the two surfaces is represented by

$$dU_{surface} = \omega_a dA \tag{1.3}$$

where dA is the differential reduction in contact area due to the propagation of an interfacial crack and ω_a is the work of adhesion between the two surfaces, defined as

$$\omega_a = \gamma_{1,air} + \gamma_{2,air} - \gamma_{1,2} \tag{1.4}$$

where $\gamma_{1,air}$ is the surface energy of surface 1 in air, $\gamma_{2,air}$ is the surface energy of surface 2 in air, and $\gamma_{1,2}$ is the interfacial energy between surfaces 1 and 2. The work of adhesion, ω_a, is the energy per unit area required to overcome van der Waals forces

between two objects. When a deformable, elastic component is introduced to the system, mechanical energy is incorporated into the total system energy

$$dU_{total} = dU_{surface} + dU_{elastic} + dU_{work} \tag{1.5}$$

where $dU_{elastic}$ is the elastic energy stored in the deformable component and dU_{work} is the mechanical work of the applied load. To describe the propagation of an interfacial crack under equilibrium ($dU_{total} = 0$), we minimize the energy stored in the mechanical system with respect to a change in interfacial contact area, dA, represented by

$$G = \frac{dU_{elastic}}{dA} + \frac{dU_{work}}{dA} \tag{1.6}$$

where G is the strain energy release rate, or the change in energy of the mechanical system per change of interfacial contact area. If G reaches a critical value, G_c, an interfacial crack will propagate; this process occurs until enough energy is released such that $G < G_c$ [15]. G_c, termed the critical strain energy release rate, is a quantity dependent on the two contacting materials. $G_c = \omega_a$ if the system is under thermodynamic equilibrium; however, experimentally there are various means of energetic loss and the measured value of G_c is usually much larger than the thermodynamic equilibrium value, ω_a [16].

1.3.2 Rate-dependent adhesion

The origins of energy loss in elastic adhesive systems have been attributed to viscoelastic losses confined to the crack tip [17], leading to a rate dependent G_c. For elastomer systems where viscoelastic losses are confined to the crack tip, the strain energy release rate can be represented by [17]

$$G = G_o \left[1 + \left(\frac{V}{V^*}\right)^n\right] \tag{1.7}$$

where G_o is the zero-velocity critical strain energy release rate, V is the velocity of the interfacial crack, V^* is a parameter related to the timescale of viscoelastic energy dissipation, and n is an empirical constant. If viscoelastic contributions are minimized (i.e., $V \ll V^*$), the strain energy release rate of Equation 1.7 approaches the thermodynamic equilibrium value of $G_o = \omega_a$. For the systems presented in the following studies, applied average strain rate is fixed within individual studies to minimize variation in crack velocity; however, crack velocity does not necessarily depend on the rate at which macroscopic stress is applied. To address this point, each of the following adhesion studies will involve an estimation or direct measurement of crack velocity to predict the contributions of rate dependent adhesion.

1.4 Bio-inspired reversible adhesion

In nature many animals, including insects, spiders, lizards, and frogs, use specialized adhesive structures for climbing, consisting of fibrillar features or smooth pads [18, 19, 20]. These specialized structures are compliant enough to make sufficient contact with ecological substrates, sometimes with the help of a secreted liquid layer [21]. In the absence of a liquid layer, referred to as dry adhesion, the forces that hold compliant adhesive structures and ecological substrates together are van der Waals forces [22]. In recent years the focus of research on reversible dry adhesion has been understanding the van der Waals-based adhesive system of the gecko, the largest organism to use adhesion for climbing. Of particular interest to engineers is the high force capacity and easy release adhesive abilities of the gecko adhesive system. It has been previously hypothesized that the main factor contributing to the high force capacity and easy release is direction-dependent fibrillar features called setae [18]. This has proven true for synthetic reversible dry adhesive systems, albeit for contact areas that are sufficiently smaller than that of the gecko (i.e., $A < 2cm^2$) [23].

Recent research has proposed and substantiated the hypothesis that fibrillar features are not necessary for high force capacity, easy release adhesives. Rather a minimally compliant adhesive system with an efficient distribution of load is more important [9, 23]. This concept is substantiated by a reversible adhesion scaling developed for adhesive systems used for climbing. The scaling is derived using an adhesion energy balance (Equation 1.5) under several assumptions [9]:

i.) the system is in thermodynamic equilibrium (i.e., $dU_{total}/dA = 0$)

ii.) the system is in a fixed displacement scenario, (i.e., $dU_{work}/dA = 0$)

iii.) the crack propagates in an unstable manner (i.e., $d^2U_{total}/dA^2 < 0$)

iii.) elastic energy is conserved (i.e., $dU_{elastic}/dA = G_c$)

The relation developed by *Bartlett et al.* takes the following form [9]:

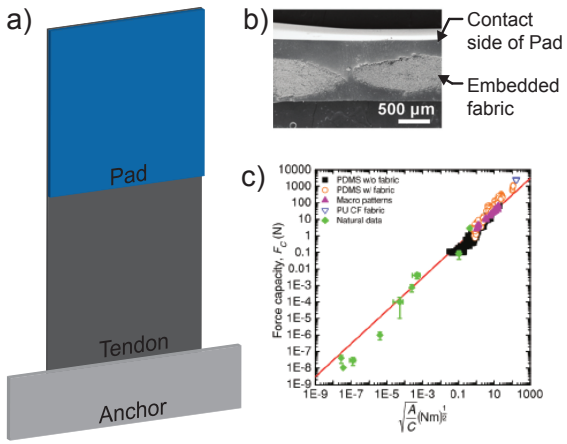

Figure 1.3. Smooth surface adhesive device. a) Schematic of reversible adhesive device. The pad is the portion of elastomer that contacts the adherend. The tendon is the portion of the fabric that is not embedded with elastomer. b) Cross section SEM of elastomer embedded fabric. c) Plot of Force capacity vs $\sqrt{A/C}$. Green data represents literature and measured values for natural reversible adhesive systems. All other data are synthetic adhesive device data featured in Ref [9]. b) and c) are adapted from Ref [9].

$$F_c = \sqrt{2G_c}\sqrt{\frac{A}{C}} \tag{1.8}$$

where F_c is the force capacity, G_c is the critical strain energy release rate, related to the specific van der Waals interactions between two contacting surfaces, A is the area of initial contact of an arbitrary shape, and C is the adhesive system compliance. This scaling proposes that maximizing adhesive contact area and minimizing compliance of the adhesive system will maximize force capacity.

Using this concept a synthetic adhesive device was developed that consists of a compliant elastomer pad embedded with a flexible fabric to maximize adhesive contact area and a stiff in-plane fabric to minimize compliance in the direction of loading (Figure 1.3a,b) [9, 24]. This device has been optimized to achieve loadings up to 3000 N for a 100cm^2 adhesive pad (Figure 1.3c) [9]. This scaling also has been shown to explain the scaling of adhesion in animals over eight orders of magnitude in size (Figure 1.3c) [9].

Recently, a study by *Gilman et al.* has investigated the relevance of this scaling for closely-related animals in the gecko family by studying the adhesion of geckos on plates of glass [25]. *Gilman et al.* found that the ratio of $\sqrt{A/C}$ explains over 90% of the variation in adhesive force capacity across seven species of gecko that vary nearly an order of magnitude in size [25], substantiating the hypothesis that minimally compliant adhesive systems are a significant factor in the scaling of adhesive force capacity of climbing organisms. The evolutionary mechanism for a less compliant adhesive system is an area of research that has not yet been explored. A key component to the evolutionary hypothesis that geckos have developed less compliant loading systems to accommodate greater adhesive force with increasing body size is the size and arrangement of tendons for the adhesive pads in the gecko. The tendons of the gecko, which are anchored to bone on one end, have been shown to be directly integrated into the skin near the adhesive pads [9, 26]. This unique arrangement is

hypothesized to be an evolutionary source of compliance control for scaling adhesive force with body size.

Although this scaling relationship of Equation 1.8 has been instrumental in the design of new synthetic adhesive systems and has provided new insight into the adhesion mechanisms of climbing organisms, many questions remain with regard to its limits and how the details of biological contacting systems can be understood for continued refinement of synthetic design. In Chapter 2 we discuss the importance of angular separation on system compliance and adhesive force capacity for multiple adhesive"digits" loaded in parallel. In Chapter 3 we address the influence of a compliant coating on the system compliance and adhesive force capacity of an isolated contact in shear.

1.5 Surface wrinkling

Wrinkling is an instability that arises from the in-plane compression of a thin film attached to a compliant substrate. There is a plethora of work that has been done to understand and control the morphology of wrinkles [27, 28, 29, 30, 31], as well work done to define the limits of the wrinkling instability [32, 33, 34, 35, 36].

An integral part of studying surface wrinkling is understanding the relations between the geometric and materials parameters that govern wrinkle feature size. When a thin film attached to a compliant substrate is compressed beyond a critical strain, the thin film will attempt to buckle out of plane. If the adhesion between the thin film and compliant substrate is sufficient, the compliant substrate must stretch to accommodate the thin film buckling. An energy balance between the thin film buckling and the compliant substrate stretching results in a periodic pattern with a minimum wavelength [37].

In the small strain limit, the minimum wavelength, λ, depends on the plane strain modulus of the film, $\overline{E}_f$, the thickness of the film, t, and the plane strain modulus of

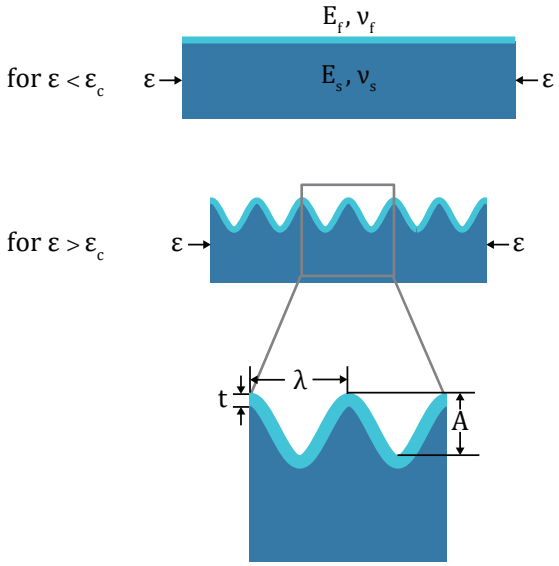

Figure 1.4. Wrinkling schematic. A strain is applied to a thin film/soft substrate composite. Beyond a critical strain (ε_c), the composite will wrinkle. The amplitude, A, and wavelength, λ, are dependent on the film thickness, t, and the film and substrate materials properties, denoted by the subscripts f and s, respectively.

the compliant substrate, $\overline{E}_s$ [38].

$$\lambda = 2\pi t \left(\frac{\overline{E}_f}{3\overline{E}_s} \right)^{1/3} \tag{1.9}$$

The critical strain, ε_c, required to wrinkle such a composite depends solely on the materials properties of the film and the substrate, as long as the modulus of the film is much greater than the modulus of the substrate [36, 38].

$$\varepsilon_c = \frac{1}{4} \left(\frac{3\overline{E}_s}{\overline{E}_f} \right)^{2/3} \tag{1.10}$$

The wrinkle amplitude, A (peak-to-valley distance), depends on applied strain to the film, ε, as well as critical strain for wrinkling and thin film thickness [38].

$$A = 2t \left(\frac{\varepsilon}{\varepsilon_c} - 1 \right)^{1/2} \tag{1.11}$$

For a fixed materials system, control of wrinkle amplitude depends only on applied compressive strain to the film. In Chapter 4, we focus on changing parameters in a plate-to-roll (P2R) film lamination process to change the applied compressive strain to the film in order to control wrinkle feature size.

1.6 Dissertation outline

This dissertation is divided up into five parts, starting with this introductory chapter, followed by three chapters reflecting on research projects, and concluding with a chapter summarizing the presented research and its scientific impact.

In Chapter 2 we fabricate a multicomponent adhesive device with multiple contact surfaces, or digits, for advancing the design of high shear capacity adhesives. Experiments are conducted to explain the relationship between adhesive digit orientation on the system compliance and adhesive force capacity of a multicomponent adhesive device. We develop analytical models to provide a framework for the performance and design of multiple contact adhesive devices, finding that the adhesive force capacity can be directly controlled by varying angular orientation between digits.

In Chapter 3 we investigate the shear deformation and reversible adhesion of a rigid flat punch contacting a soft, laterally-extensive elastomer layer. We investigate the scaling of shear compliance, C, with the ratio of contact radius to elastomer layer thickness, or confinement ratio (a/h), through both experiment and finite element analysis. Using a reversible adhesion scaling analysis, we also investigate the relationship between the shear adhesion force capacity, F_c, and the confinement ratio using experiments.

In Chapter 4 we present and develop a patterning technique that relies on the contact mechanics and geometry of rolling to create mechanically tunable wrinkled surface structures. A plate-to-roll (P2R) geometry is used to laminate a thin film onto a soft substrate. During this process the deformation of the soft substrate

due to contact load, as well as deformation due to bending around the roller, can induce wrinkling. Importantly, we demonstrate that the amplitude of wrinkles can be controlled by applied contact load and roller curvature. We demonstrate this using a 150nm poly(styrene) thin film supported on a silicon wafer and a 2mm thick poly(dimethyl siloxane) rubber substrate. We develop semi-empirical equations to describe the effect of applied contact load and roller curvature on the wrinkle aspect ratio. To support experimental relationships between contact conditions and strain at the roll/plate interface, finite element modeling (FEM) of a soft substrate in full-friction rolling contact with a rigid plate is conducted.

CHAPTER 2

INFLUENCE OF DIGIT ANGLE ON ADHESIVE FORCE

2.1 Introduction

In this study we fabricated a multicomponent adhesive device with multiple contact surfaces, or digits, for advancing the design of high shear capacity adhesives. Experiments are conducted to explain the relationship between adhesive digit orientation on the system compliance and adhesive force capacity of a multi-component adhesive device. We develop analytical models to provide a framework for the performance and design of adhesive devices with multiple contacts, finding that the adhesive force capacity can be directly controlled by varying angular orientation between digits. The explicit relationship of system compliance in a multiple digit setup depends directly and non-linearly on the angular orientation between digits. We also find that the adhesive force capacity in a multiple digit setup depends inversely and non-linearly on the angular orientation between digits. These findings can lead to more complex adhesive device design, as well as guide biomechanical analyses of climbing organisms with similar adhesive component arrangements.

2.2 Background

2.2.1 Previous work on bio-inspired fabric-elastomer adhesives

Bio-inspired adhesive design involves understanding examples of natural adhesive systems and adapting chemistries or concepts into engineered, functional designs, leading to creative solutions in the adhesives industry. Semi-permanent adhesive systems like that of the mussel rely on metal-coordination chemistries to exploit specific

interactions between surfaces, creating intermolecular forces that can be tuned via pH, leading to high force capacity glues that are resistant to rough tidal conditions [39]. Locomotive adhesive systems like that of the gecko rely on very weak intermolecular forces between surfaces to create adhesion. But they are designed in such a way to make large areas of contact and transfer load efficiently to the interface, leading to high force capacity, easy release adhesion [40]. The system of the gecko includes a variety of components with varying modulus, stiffness, and geometric arrangement to achieve a design that effectively transfers load from the animal to the interface.

When studying the adhesion of natural systems, most of the components far from the interface are neglected. The compliance of components far from an adhesive interface have been shown to alter the adhesive force in synthetic systems [9, 41] and recently have been shown to impact the adhesive force in natural systems [25]. This concept led to the design and refinement of bio-inspired, high force capacity fabric-elastomer adhesives that are reversibly removable [9, 24, 42, 43, 44]. The bio-inspiration element of this previous work lies in replicating a unique concept of load bearing abilities within the gecko's adhesive system - a flexible and conformal system in the direction of contact (replicated by a soft elastomer coating with a flexible fabric backing) and a stiff series of components in the direction of loading (replicated by the shearing of a thin elastomer layer impregnated with stiff, planar fabric). This concept was developed based on a reversible adhesion scaling [9]

$$F_c \sim \sqrt{G_c}\sqrt{\frac{A}{C}} \tag{2.1}$$

where adhesive force capacity, F_c, is described by the ratio of contact area to system compliance in the loading direction, A/C, and the critical strain energy release rate, G_c. This reversible adhesion scaling has been substantiated experimentally by explaining the performance of synthetic adhesive systems [9, 24, 43], as well as natural adhesive systems [9, 25]. Furthermore, Equation 2.1 has led to the design of more

complex, multicomponent systems for engineering device optimization [24, 42, 44, 45], and the construction of synthetic models to provide feedback into the study of natural adhesive systems [25, 42]. Focusing on both complex adhesive device design and feedback into the study of natural adhesive systems, here we present a new concept for controlling adhesive force capacity in a multicomponent adhesive system with multiple contact surfaces, or "digits", by investigating the influence of angular spacing between adhesive components.

2.2.2 Sources of adhesion control in climbing animals

The inspiration for this device design arises from observations of geckos statically hanging on vertical substrates. Previous research on the forces geckos exert on substrates during locomotion has focused on measuring reaction forces and studying locomotive gait of geckos on inclined surfaces [46, 47], and how adhesive digit orientation changes when the lizard is actively climbing uphill or downhill [48, 49]. Here, we highlight unpublished work by *Kuo et al.*, shown in Figure 2.1, which is focused on observing the posture of *Gekkonidae* lizards statically hanging on glass substrates that are oriented with the direction of gravity [50]. This unpublished data has yet to be analyzed in detail from a biological perspective. However, it inspired the question of how digit angle can influence adhesive force capacity.

In this specific scenario a gecko has climbed vertically up a plate of glass. The gecko's center of mass is in equilibrium, where the adhesive force exhibited on the glass substrate is balanced by the gravitational force on the center of mass. The ability of the gecko to move away from the ground depends on the movement of its center of mass in relation to the glass substrate, the strength and angular orientation of its musculoskeletal system, the strength of its adhesive structures, and the movement of the substrate. Based on observations of statically hanging animals in Figure 2.1, the *G. vittatus* specimen in Figure 2.1a, with the fore-aft axis of its body directed up,

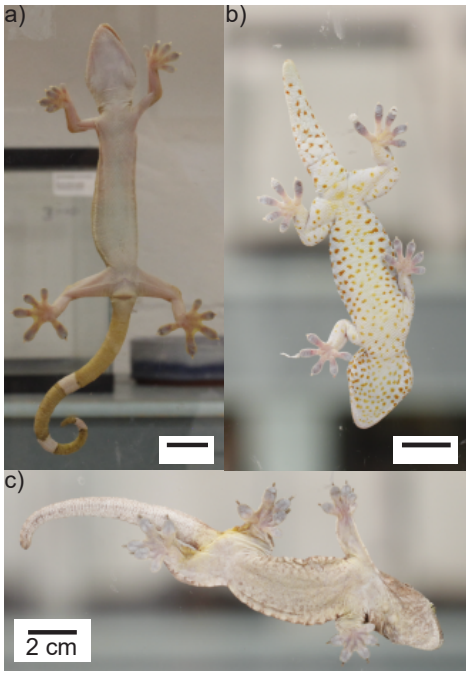

Figure 2.1. Various species of gecko hanging on a vertically-oriented glass pane [50]. Fore-aft refers to the snout-to-vent axis of the animal. Orientation direction refers to the direction with respect to gravity. a) *G.vittatus* with a fore-aft, up orientation. b) *G.gecko* with a fore-aft down orientation. c) *G.vorax* with a fore-aft, horizontal orientation

away from the direction of loading (direction of gravitational force), has a posture that is ready to move to oppose the loading direction. The forelimb adhesive digits are aligned up and the hindlimb adhesive digits are spread out and oriented down. We hypothesize that for locomotion which opposes loading, the degree of alignment of adhesive components in the direction of loading are maximized. Additionally, for providing load support and bracing during climbing, hindlimb digits are splayed to provide resistance to slip.

For postures that are not oriented such that the animal can readily locomote to oppose loading, we hypothesize that animals will organize their adhesive digits in such a way that does not optimize adhesive force in the loading direction but rather provides a more than sufficient amount of resistance against the load. *G. gecko* and *G. vorax* of Figure 2.1b and c, respectively, have body orientations such that their fore-

aft body axes are not aligned with the direction of gravity - they are in an orientation less poised to move away from the loading direction. Additionally, they both have at least three sets of digits oriented to oppose the loading direction and almost all digits spread out. These observations led to one main hypothesis: the angular orientation of adhesive components (digits and limbs) directly controls the maximum adhesive force achievable in the direction of loading. Throughout this study a synthetic model will highlight explicit relationships between adhesive digit orientation and the system compliance and adhesive force capacity in the direction of loading.

2.3 Approach

This bio-inspired adhesive device study utilizes an arrangement of adhesive components where three identical digits are adhered to a substrate and loaded simultaneously. Changing digit orientation is a strategy to change system compliance in the direction of loading, which has been shown in other systems to impact adhesive force capacity. System compliance is the collective compliance of components in the adhesive system, where the increase of the compliance of a single digit can augment the compliance of the entire system. Here, a systematic variation of outer digit orientation relative to a center digit is conducted to determine its effect on system compliance. Additionally, the effect of outer digit orientation in a multiple contact adhesive system on adhesive force capacity is highlighted. Understanding the degree to which spreading out digits influences adhesive device performance will lead to more complex adhesive device designs and further development of biomechanics models for natural adhesive systems. First, synthetic adhesive digits are fabricated, consisting of an elastomer contact surface and a flexible, stiff fabric for applying load across the contact surface. Second, the compliance and force capacity of each individual digit is characterized for reference during analysis of the three digit device setup. Third, the three adhesive digits are loaded simultaneously to determine the compliance and

force capacity of the loading system with a specified orientation. This system is then subject to different orientations to make clear the effect of angular spacing on three digit adhesive device performance.

2.4 Experimental

2.4.1 Device fabrication

A two-part siloxane-based elastomer [SYLGARD® 184, Dow Corning, Inc.] is mixed in a 10:1 ratio of pre-polymer to cross-linker, degassed for 10 min, and poured into a 100x100x1mm plate glass mold. A plain-weave nylon fabric [95 gsm, JoAnn Fabrics] is used as received, cut to size, and placed over the uncured elastomer. The sample is cured at 20°C for 120hrs. Fabric-elastomer samples were cut to size, as shown in Figure 2.3a, where the length of the fabric as cut is the fill direction. Polycarbonate pieces [Makrolon®, Covestro AG] were cut to size and glued to the bottom of the fabric using a cyanoacrylate super glue [Loctite®, Henkel Corp.] to act as an attachment point, called an anchor. The wrist was 3D printed using ABS plastic from a fused-filament fabrication 3D printer [Dimension uPrintSE Plus, Stratasys, Inc.]. The 3D printed wrist was marked with rules between 0° and 90° in 15° increments (Figure 2.2a).

2.4.2 Device testing

Lap shear tests of three synthetic adhesive "digits" adhered to a polycarbonate substrate [Makrolon®, Covestro AG] loaded simultaneously were measured using an Instron 5564 tensile testing machine. Three adhesive digits anchored by a "wrist" (Figure 2.2a) were loaded, where the center digit was kept parallel to the loading direction and the angle of the outer adhesive digits were varied. Tests were conducted at 10 mm/min. Force-displacement data were analyzed to define the adhesive force capacity and the compliance of the testing system. The force capacity is the force at

adhesive failure, indicated by the dashed line in Figure 2.2b. The compliance of the testing system is measured by taking the inverse of the slope of the loading curve, indicated by the solid line in Figure 2.2b. A linear fit is applied to the force-displacement data between two user defined data points. The initial point qualitatively corresponds to the point at which all three digits are loaded simultaneously. The final point is the force at adhesive failure.

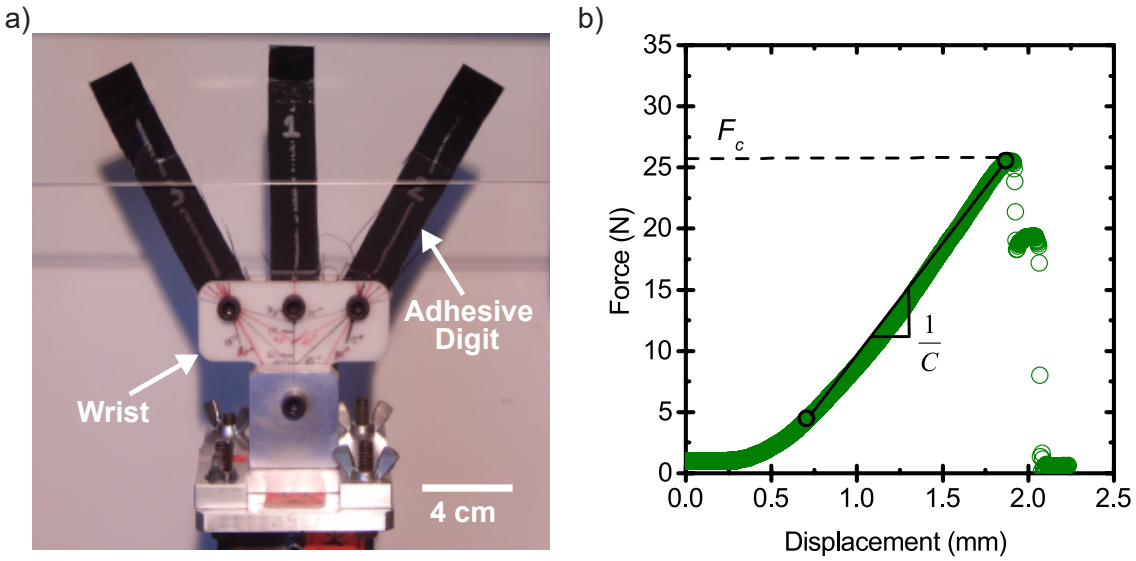

Figure 2.2. Three-digit adhesive device and testing. a) Schematic of adhesive digit testing setup. Three adhesive "digits" are attached to a "wrist", which is secured to the bottom of the testing setup. Using markings on the wrist, the angular spacing between digits is set during attachment onto a plate of polycarbonate. The polycarbonate is attached to a displacement actuator and a force sensor to load the device. b) Representative force-displacement curve highlighting F_c, the adhesive force capacity, and C, the compliance of the testing system.

2.5 Individual digit characterization

2.5.1 Individual digit structure and compliance

An adhesive digit consists of an elastomer pad and a fabric tendon, as shown in Figure 2.3a. Each individual digit is loaded in the setup shown in Figure 2.2a and the force capacity and compliance in the direction of loading are quantified as described

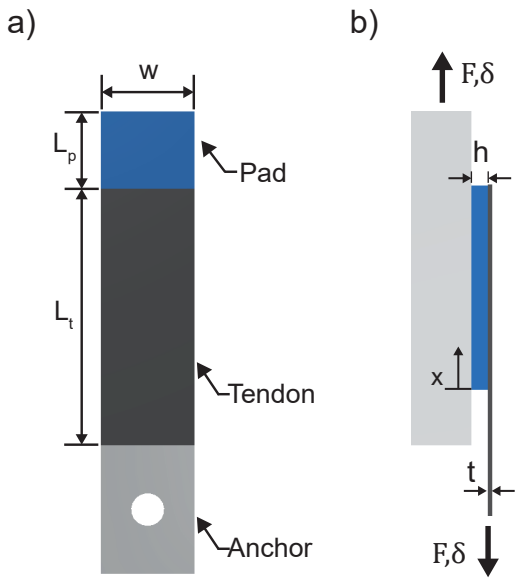

Figure 2.3. Synthetic adhesive digit design. a) Synthetic adhesive digit dimensions. The pad is the region of fabric embedded with elastomer. The tendon is the region of pure fabric. b) Synthetic adhesive digit loading.

previously. The results are recorded in Table 2.2. For an individual digit, the compliance is dependent on both the elastomer deformation and the fabric deformation. Analytical expressions for the compliance of multiple components of fabric-elastomer adhesive devices have been shown previously [44], including direct relations of materials properties and geometry. In this study, the compliance of the pad and tendon are investigated, as well as the compliance of the skin - the portion of fabric embedded with elastomer. The compliance of an elastomer pad in shear has been previously described using a shear block relation:

$$C_{pad} = \frac{h}{wL_p\mu} \tag{2.2}$$

where h is the elastomer thickness, L_p is the length of the pad, w is the width of the pad, and μ is the shear modulus of the pad. The compliance of a fabric tendon in extension has been previously described using a uniaxial extension equation:

$$C_{tendon} = \frac{L_t}{twE} \tag{2.3}$$

where L_t is the length of the tendon, t is the thickness of the fabric, w is the width of the tendon, and E is the effective Young's modulus of the fabric. The compliance of a fabric-elastomer skin in extension has been previously described using a uniaxial extension equation:

$$C_{skin} = \frac{L_p}{twE^*} \tag{2.4}$$

where L_p is the length of the pad, t is the thickness of the fabric, w is the width of the tendon, and E^* is the composite modulus of the fabric-elastomer. Relevant geometric parameters used in this study are summarized in Table 2.1.

w (mm)	L_p **(mm)**	L_t **(mm)**	**h (mm)**	**t (mm)**
18	15	50	1.2	0.2

Table 2.1. Experimental geometries for individual digits.

2.5.2 Compliance of device components

To highlight contributions of individual components to the overall compliance of an adhesive digit, the compliance of each component is either calculated (i.e., pad and skin) or directly measured (tendon). The results for this analysis are recorded in Table 2.2. To calculate compliance of the pad and skin, measured geometric parameters and materials properties are first quantified.

For the elastomer, a Young's modulus of $E = 1.02$ MPa (± 0.03 MPa standard deviation, n=8) and a critical strain energy release rate of $G_c = 0.19 \pm 0.03$ J/m^2 are reported from normal adhesion (tack) tests on independent samples of elastomer prepared under identical curing conditions. Tack tests are conducted using a 4.71mm radius glass hemispherical probe indenting a 2.47mm thick slab of elastomer at a rate of $10\mu m/s$. A custom-built contact adhesion testing setup is used, consisting of a displacement actuator [Inchworm 8300, Burleigh Instruments], a microscope for

Component	C (mm/N)	E (MPa)	F_c (N)
Elastomer pad	0.012	1.02±0.03	-
Fabric tendon (fill)	0.096±0.004	145	-
Fabric tendon (warp)	0.036±0.001	371	-
Fabric skin (fill)	0.029	145*	-
Center digit	0.125±0.006	-	8.76±1.04
Right digit	0.133±0.005	-	7.55±1.22
Left digit	0.135±0.006	-	6.69±1.05

Table 2.2. Results of component and single digit testing. Compliance values, C, are either calculated using Equations 2.2 or 2.4 (elastomer pad and fabric-elastomer skin, respectively) or directly measured in the Instron 5564 setup (fabric tendon). Elastic modulus values, E, are determined from either a tack test (elastomer pad) or calculated using the stiffness from tensile tests and the cross-sectional geometry (fabric). Tensile tests are conducted for n=5 fabric samples in both the warp and fill directions. We report the mean values with the standard deviation. Adhesive force capacity, F_c, is determined from lap shear tests.

imaging contact area [Zeiss Axiovert 200M], and a custom-built single capacitor-aluminum cantilever load cell [PISeca D-510.020 single-electrode capacitive sensor and PISeca E-852.10 signal conditioner, Physik Instrumente, GmbH]. Elastomer modulus and critical strain energy release rate are determined using a JKR analysis [16]. The following equations are used to determine modulus [16]:

$$P = E^* \left\{ \frac{4a^3}{3R} f_p - 2a f_c \left(\frac{a^2}{R} f_\delta - \delta \right) \right\} \tag{2.5}$$

where P is applied load, E^* is the plane strain modulus of the elastomer, a is the contact radius, R is the radius of the probe, δ is the displacement, and f_p, f_c, and f_δ are corrections for the load, compliance, and displacement relations due to confinement, defined as

$$f_p = \left(1 + 0.33 \left(\frac{a}{h} \right)^3 \right) \tag{2.6}$$

$$f_c = \left(1 + 1.33 \left(\frac{a}{h} \right) + 1.33 \left(\frac{a}{h} \right)^3 \right)^{-1} \tag{2.7}$$

$$f_\delta = \left(0.4 + 0.6 \exp \left(\frac{-1.8a}{h} \right) \right) \tag{2.8}$$

where h is the thickness of the elastomer layer. To determine E, we plot P with the right hand side of Equation 2.5 and find the slope of the indentation portion of the curve. The slop corresponds to the plane strain modulus of the elastomer, $E*$, which is defined as $E^* = E/(1-\nu^2)$. To determine G_c, we use the following relation [16]:

$$G = \frac{\left(\frac{4a^3E^*}{3R}f_p - P\right)^2}{8\pi E^* a^3} f_{Gp} \tag{2.9}$$

where G is the strain energy release rate and f_{Gp} is the correction factor to account for confinement, defined as

$$f_{Gp} = \left(\frac{0.56 + 1.5\left(\frac{a}{h}\right) + 3\left(\frac{a}{h}\right)^3}{\left(0.75 + \left(\frac{a}{h}\right) + \left(\frac{a}{h}\right)^3\right)^2} \right) \tag{2.10}$$

The reported G_c corresponds to the value of G calculated using Equation 2.9 with input parameters of the maximum tensile load and corresponding area. These values are used to capture the maximum G_c achieved with this tack loading and geometry for qualitative comparison to G_c values under loading conditions of this experimental adhesive digits study.

For the effective modulus of the fabric, independent tensile tests using a sample of nylon fabric are conducted using an Instron 5564 testing apparatus. Figure 2.4a presents five replicates of force-displacement curves for the fabric in both the warp direction and the fill direction. A linear fit is applied to the data to determine the stiffness for the fabric in both the fill and warp directions. As expected, the tensile stiffness of the fabric in the warp direction is different from that in the fill direction [51]. Fabric stiffness in orthogonal directions may vary on the processing conditions during weaving, or even post-processing conditions. For a plain-weave fabric, there are many sources for variation of tensile properties in orthogonal directions, including yarn twist and crimp. Yarn twist is the amount of torsion applied to a bundle

of fibers, or yarns, before placing in the loom, which in turn can change the tensile stiffness of the yarn. Crimp is the degree to which yarns are bent to accommodate the weaving process. Depending on how much tension is placed on the warp yarns during weaving, this can change the amount of fabric crimp in the warp direction. Additionally, post-processing techniques such as calendering can change the stiffness of the fabric through decrimping. Decrimping is the straightening of bent yarns that are woven over-and-under orthogonal yarns. In this sample, the load-displacement curve

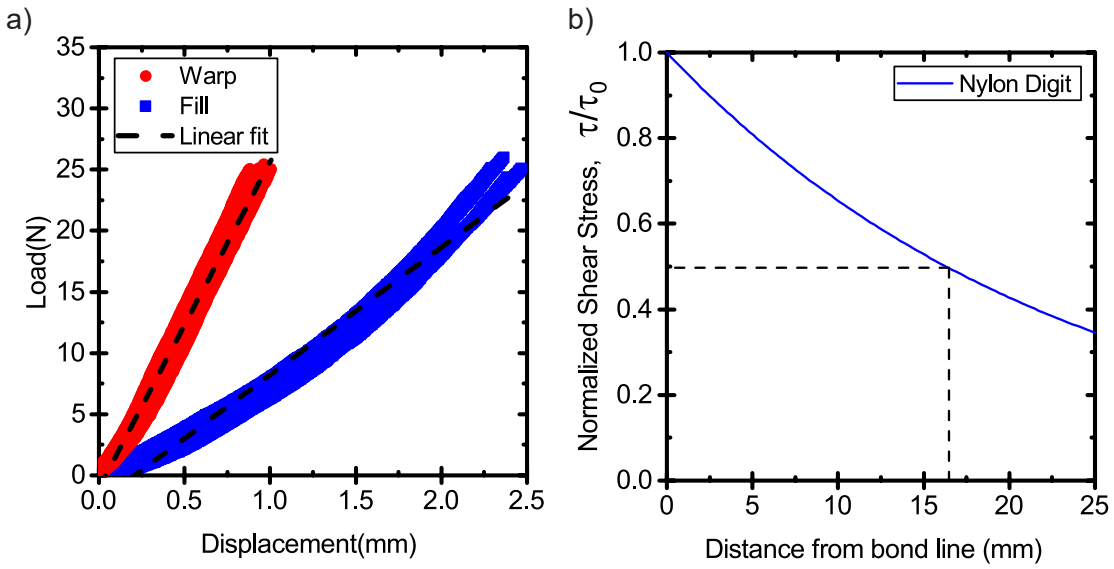

Figure 2.4. Digit component analysis. a) Load-displacement curve of fabric in warp (red) and fill (blue) directions. Linear fits are applied to the fabric extension data, represented by the dashed black lines to determine an effective tensile modulus, E. b)Shear stress decay of an adhesive lap joint. Using the geometry and materials properties of this system, the shear stress decay is calculated using Equation 2.11. Dashed black lines represent the point of 50% reduction in shear stress at the interface.

for the warp direction shows a generally linear trend, devoid of an initial decrimping region, most likely the result of post-processing (Figure 2.4a). The load-displacement curve for the fill direction has a region of low stiffness, followed by a region of higher stiffness (Figure 2.4a). This initial region of low stiffness is attributed to decrimping, whereas the following region is attributed to yarn extension. For the adhesive digits in this study, the fabric is cut such that the fill direction is along the main axis of

the adhesive digit. The linear fit for the fill fabric of Figure 2.4a does not capture the trend of the data; however, we use the linear elastic approximation to simplify equations for capturing trends of compliance and force capacity, and for making approximations for shear stress decay length. Using the compliance measured from these independent tensile tests, an effective tensile modulus of the fabric can be calculated by considering cross-sectional geometry.

The compliances of the elastomer pad in shear, the fabric tendon in extension, and the fabric-elastomer of the skin in extension approximately equal the compliance measured of individual digits adhered to polycarbonate. Previous calculations of skin compliance consider the fabric-elastomer via a composite modulus, E^*, using a Voigt model [44]. Here, the compliance of the skin is calculated such that the modulus of the elastomer is ignored for the purpose of a qualitative comparison between calculated compliance and measured compliance. Thus, in Table 2.2 the modulus of the skin reported is the effective modulus of the fabric in extension.

2.5.3 Shear stress decay

In the specific mechanical loading of adhesive digits, referred to as lap joint testing, the extension of the backing can result in a decay of shear stress. This decay arises from a lag of stress transferred from the extensible backing to the interface. The adhesive is loaded from the bottom of the tendon contact, designated as $x = 0$ in Figure 2.3b, to the top. The shear stress that develops at the interface will decay in the x-direction according to the relation [52]

$$\tau/\tau_o = e^{-\alpha x}; \quad \alpha = \left(\frac{\mu}{htE}\right)^{1/2} \tag{2.11}$$

where τ/τ_o is the normalized shear stress and x is the distance from the bond line. Using measured values from Tables 2.1 and 2.2, the shear stress decay for a nylon fabric backing and a PDMS elastomer adhesive layer is calculated and shown in

Figure 2.4b. From this calculated curve, the adhesive digit geometry in this study ($L_p = 15$mm) is chosen such that the shear stress does not fall below 50% along the length of the pad.

2.6 Results and discussion

2.6.1 Influence of digit angles on system compliance

The change in system compliance, C_{sys}, as a function of angular orientation, θ, is presented in Figure 2.5a. As the angle between digits is increased, the compliance of the system increases. To explicitly describe this trend, we implement a two-dimensional vector analysis of the three-digit system before and after load is applied. A schematic of the three-digit setup attached to a substrate is presented in Figure 2.5b. We present an idealized model of the three-digit system (Figure 2.5c), where each digit is considered to be a tension member pinned at adhesive contact. Force transmission through the system is examined using a free-body diagram (Figure 2.5d), assuming quasi-static equilibrium and small displacements such that each member is considered a rigid body. Using the free-body diagram, the sum of the forces in the x-direction are represented as

$$\underline{\sum F_x = 0:} \;\; F_2 \; sin\,(\theta_{12}) = F_3 \; sin\,(\theta_{13}) \tag{2.12}$$

where F_2 is the force transmitted through the right digit, F_3 is the force transmitted through the left digit, θ_{12} is the angular orientation between the right and middle digit, and θ_{13} is the angular orientation between the left and middle digits. The sum of the forces in the y-direction are represented as

$$\underline{\sum F_y = 0:} \;\; F_{sys} = F_1 + F_2 \; cos\,(\theta_{12}) + F_3 \; cos\,(\theta_{13}) \tag{2.13}$$

where F_{sys} is the force applied to the three-digit system and F_1 is the force transmitted through the middle digit. To describe the compliance of the system, assuming all

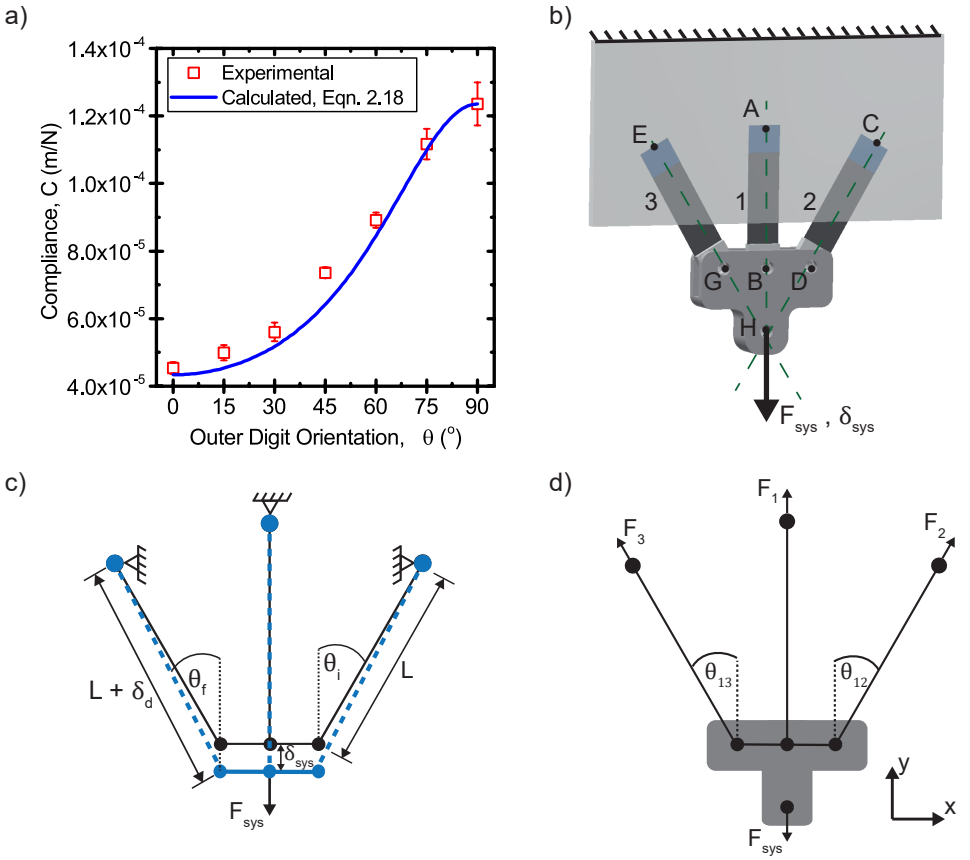

Figure 2.5. Three-digit adhesive device deformation. a) Compliance vs. outer digit orientation, θ. Open red square data represent experimentally measured values and the solid blue line represents the calculated compliance of Equation 2.18 using values of individual digit compliance from single-digit tests. b) Schematic of the three-digit adhesive device. A displacement, δ_{sys} is applied to the adhesive system, transmitting a force, F_{sys} throughout the system. c) Undeformed geometry (solid black lines) and deformed geometry (dashed blue lines). d) Free-body diagram of a three-digit adhesive device.

components are linear-elastic, we substitute δ/C for each of the force components of Equation 2.13, leading to the following relation

$$\frac{\delta_{sys}}{C_{sys}} = \frac{\delta_1}{C_1} + \frac{\delta_2}{C_2}\, cos\,(\theta_{12}) + \frac{\delta_3}{C_3}\, cos\,(\theta_{13}) \tag{2.14}$$

where δ_{sys} is the displacement of the entire system in the load direction, C_{sys} is the compliance of the system in the load direction, δ_n/C_n for n=1, 2, and 3 represent the ratio of displacement to compliance along the length of the digit for the middle, right, and left digits, respectively. Solving for C_{sys}, we find the following relation that describes the system compliance

$$C_{sys} = \left\{ \frac{1}{C_1} + \frac{\delta_2}{C_2 \delta_{sys}} \, cos\left(\theta_{12}\right) + \frac{\delta_3}{C_3 \delta_{sys}} \, cos\left(\theta_{13}\right) \right\}^{-1} \tag{2.15}$$

Equation 2.15 is a generalized relation for a three-digit system with components of varied compliance and angular orientation. Here, displacements in the direction of loading are equivalent for all digits, so δ_{sys}=δ_1. To represent our experimental conditions, we simplify the system compliance relation such that θ_{12}=θ_{13}=θ_f, C_1=C_2=C_3=C_d, and δ_2=δ_3=δ_d, resulting in the following relation

$$C_{sys} = \left\{ \frac{1}{C_d} + 2\frac{\delta_d}{C_d \delta_{sys}} \, cos\left(\theta_f\right) \right\}^{-1} \tag{2.16}$$

where C_d is the compliance of an individual digit, δ_d is the displacement of an outer digit parallel to its length, and θ_f is the angle between an outer digit and the center digit after loading. δ_d can be defined in terms of known system geometry,

$$\delta_d = \delta_{sys} \, cos\left(\theta_f\right) \tag{2.17}$$

If the system displacement is small relative to the initial digit length ($\delta_{sys}/L \ll 1$), we can assume a small displacement condition. Due to the uncertainty in θ_i during experiments ($\pm 2^{o}$) and the assumption of small system displacement, $\theta_f \approx \theta_i$. Using these assumptions and inserting Equation 2.17 into Equation 2.16, the simplified expression for total system compliance in the direction of loading becomes

$$C_{sys} = \left\{ \frac{1}{C_d} + 2\frac{1}{C_d} cos^2\left(\theta_i\right) \right\}^{-1} \tag{2.18}$$

The total compliance as a function of outer digit orientation is calculated using experimental values from Table 2.2 and inserting them into Equation 2.18. The calculated compliance correlates well with the experimental data, as shown by the solid blue curve in Figure 2.5a.

2.6.2 Active control of reversible adhesive force

Following the scaling of Equation 2.1, the compliance of an adhesive testing system directly influences adhesive force capacity. In this experimental setup, the angular spacing of the adhesive digits acts as a way to control adhesive force capacity via a change in compliance. Figure 2.6 represents data obtained from experiments describing the influence of outer digit orientation on adhesive force capacity. Figure 2.6a highlights the scaling of adhesive force capacity with the ratio of measured contact area to measured compliance in the loading direction. For small angles, a general agreement is shown with the scaling 0.5 from Equation 2.1. However, for larger angular orientations, this type of scaling analysis breaks down.

Equation 2.1 was derived assuming when the force in the adhesive system, F_{sys}, reaches a critical value, $F_{c,sys}$, the entire adhesive contact area, A, fails in one step. In our adhesive system, we consider failure to be when a single adhesive surface fails completely; however, force is transferred through all three adhesive digits over three adhesive areas. The force in the three-digit adhesive system before adhesive failure is presented by Equation 2.13, determined from the free-body diagram of Figure 2.5d. The force of the system reaches a critical value when a single component reaches its critical value. If we first focus on failure of only the middle digit, the force capacity of the middle digit is represented as

$$F_{c,1} = \sqrt{2G_{c,1}}\sqrt{\frac{A_1}{C_1}} \tag{2.19}$$

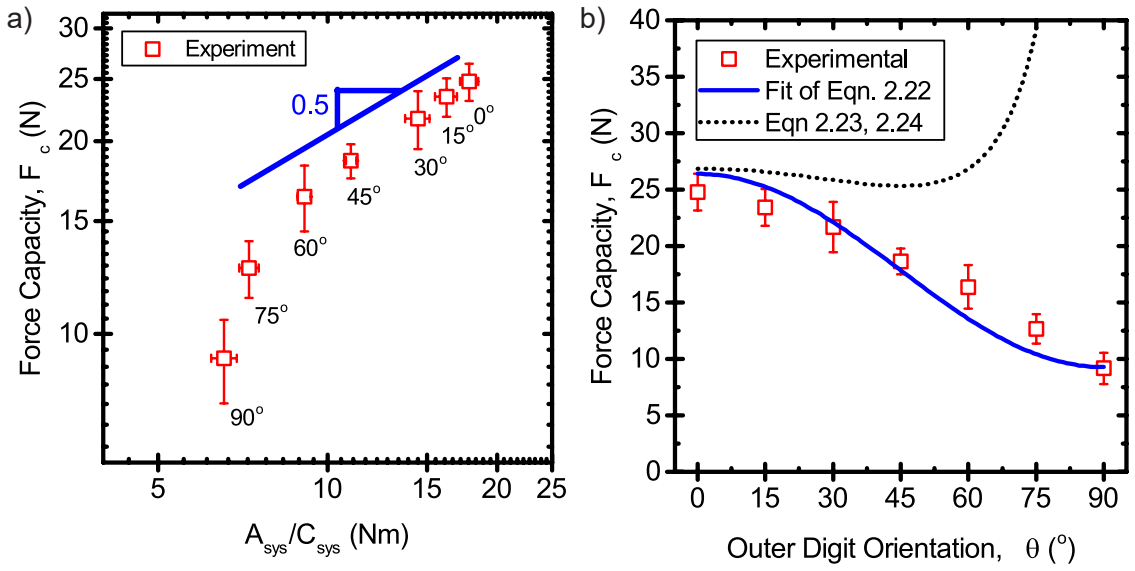

Figure 2.6. Three-digit adhesive device force capacity. a) Plot of Force capacity, F_c, vs. adhesive area of the system and system compliance in the direction of loading, A_{sys}/C_{sys}. Open red square data represent experimentally measured values and the solid blue line represents a line with a slope of 0.5. b) Force capacity vs. outer digit orientation, θ_i. Open red square data represent experimentally measured values and the solid blue line represents a fit of Equation 2.22. The dotted black line represents Equations 2.23 and 2.24.

where $G_{c,1}$ is the critical strain energy release rate of the middle digit, A_1 is the area of contact of the middle digit, and C_1 is the individual compliance of the middle digit. If we insert Equation 2.19 into Equation 2.13, we find

$$F_{c,sys,1} = \sqrt{2G_{c,1}}\sqrt{\frac{A_1}{C_1}} + F_2 cos\left(\theta_{12}\right) + F_3 cos\left(\theta_{13}\right) \tag{2.20}$$

where $F_{c,sys,1}$ is the critical force reached in the three-digit system for adhesive failure of the middle digit, F_2 is the force transferred through the right digit, and F_3 is the force transferred through the left digit. To describe F_2 and F_3 in terms of known quantities such as the individual digit compliances, C_2 and C_3, and outer digit angular orientations, θ_{12} and θ_{13}, we consider the force transmitted through an individual digit as $F_d = \delta_d/C_d$. Using the relation of Equation 2.17, which describes the displacement of an individual digit in terms of the system displacement, Equation 2.20 becomes

$$F_{c,sys,1} = \sqrt{2G_{c,1}}\sqrt{\frac{A_1}{C_1}} + \frac{\delta_{sys}}{C_2}cos^2\left(\theta_{12}\right) + \frac{\delta_{sys}}{C_3}cos^2\left(\theta_{13}\right) \tag{2.21}$$

If we substitute $\delta_{sys} = F_{c,sys}C_{sys}$ into Equation 2.21, the relation of force capacity of the three-digit system for middle digit failure becomes

$$F_{c,sys,1} = \sqrt{2G_{c,1}}\sqrt{\frac{A_1}{C_1}}\ \left[1 - \frac{C_{sys}}{C_2}cos^2\left(\theta_{12}\right) - \frac{C_{sys}}{C_3}cos^2\left(\theta_{13}\right)\right]^{-1} \tag{2.22}$$

Equation 2.22 represents the force capacity of the three-digit system where the middle digit fails first, highlighting the influence of individual digit compliance, angular spacing, and system compliance. For systems where the middle digit may not be the first to fail, we derive force capacity equations for the right and left digits in an analogous manner,

$$F_{c,sys,2} = \sqrt{2G_{c,2}}\sqrt{\frac{A_2}{C_2}}\ cos\left(\theta_{12}\right)\left[1 - \frac{C_{sys}}{C_1} - \frac{C_{sys}}{C_3}cos^2\left(\theta_{13}\right)\right]^{-1} \tag{2.23}$$

$$F_{c,sys,3} = \sqrt{2G_{c,3}}\sqrt{\frac{A_3}{C_3}}\ cos\left(\theta_{13}\right)\left[1 - \frac{C_{sys}}{C_1} - \frac{C_{sys}}{C_2}cos^2\left(\theta_{12}\right)\right]^{-1} \tag{2.24}$$

where $F_{c,sys,2}$ is the force capacity of the three-digit system where the right digit fails first, and $F_{c,sys,3}$ is the force capacity of the three-digit system where the left digit fails first. Equations 2.22-2.24 represent the criteria for adhesive failure of a single digit in a three-digit system, of which the lowest $F_{c,sys}$ is the first criterion met in the adhesive system.

In our system we assume $G_{c,1} = G_{c,2} = G_{c,3} = G_c,\ C_1 = C_2 = C_3,\ A_1 = A_2 = A_3$, and $\theta_{12} = \theta_{13}$. For this set of assumptions $F_{c,sys,1}$ is the lowest of the three criteria of Equations 2.22- 2.24 for $\theta > 0$. Using this criterion Equation 2.22 is fit to the experimental data in Figure 2.6b by a single parameter, G_c, showing good agreement. We find the fit value of $G_c = 19.7$ J/m^2 to be significantly larger than the G_c for this elastomer in the normal direction using independent tack tests. A discussion of this

difference is presented in the following section. Equations 2.23 and 2.24 are calculated using the fit value of G_c and plotted with the experimental data in Figure 2.6b, showing significant departure at angles larger than 30°.

The relations of Equations 2.22- 2.24 have several implications for adhesive device design. The force capacity of a system with multiple adhesive contacts loaded in parallel can be explicitly described for components with varied area, G_c, compliance, or a combination of these. Using these relations as a design tool, area, G_c, compliance, or angular spacing can be tuned to achieve predictable force capacities. As an example, we incorporate the critical strain energy release rate, G_c, of the adhesive system into our explicit equations, which will lead to more complex device optimization such as tailoring materials properties of the adhesive pads for use on "real world" surfaces, as previously described by *King et al.* [24].

Additionally, Equations 2.22- 2.24 have malleability to adapt to existing reversible adhesive systems where numerous adhesive contacts are loaded in parallel [23, 42]. In our study, we use θ as a tool to vary compliance of the adhesive system and observe its impact on adhesive force capacity. Other studies, including *Bartlett et al.* and *Hawkes et al.*, present experiments where compliances of individual adhesive contacts have inherent variation, leading to a variation in adhesive force capacity of the entire system [23, 42]. The equations developed in our study provide a foundation to use the variation of individual digit compliance to predict overall adhesive device performance.

Equations 2.22- 2.24 also have applicability for animal biomechanics studies. The variability in angular spacing between adhesive digits is explicitly related to the variability in system compliance using Equation 2.18. Furthermore, Equations 2.22- 2.24 explicitly define the variability in adhesive force capacity as the result of variation in angular spacing between digits. For the studies previously conducted on the orientation of gecko adhesive digits during locomotion on inclined substrates [48, 49], the

equations presented here explicitly define the penalty in adhesive force capacity when adhesive digits have large angular separations.

2.6.3 G_c for shear loading in a three-digit system

The fit value of $G_c = 19.7$ J/m^2 is two orders of magnitude larger than the G_c measured in the normal direction during independent tack tests. This large difference in critical strain energy release rate of shear loading compared to normal loading has been seen previously in elastomeric systems. The large difference seen here can be attributed to frictional energy dissipation, mode of stress transfer, rate dependent adhesion, or a combination of these.

First, in similar shear loading geometries the presence of microslip has been observed experimentally, even in the absence of macroscopic relative translation between the two surfaces [53]. In these cases an increase in G_c has been recorded, attributed to the presence of microslip causing frictional energy dissipation. Second, the critical strain energy release rate for pure, mode II shear failure is known to be considerably larger for many polymer interfaces. Although we cannot confirm the exact stress distribution at the interface in these experiments, the shear stress decay model presented above suggests that significant shear stresses exist within the interfacial area. Therefore, these shear stresses likely lead to mode mixity of failure, different than pure mode I, hence leading to an increased G_c. Finally, the rate dependence of adhesion for cross-linked elastomers has been shown previously to influence G_c [54]. The samples presented here are designed to transfer stress in such a way that "unstable" failure occurs between the adhesive and the adherend, leading to rates of crack propagation orders of magnitude faster than the stress loading rate. The rate of crack propagation in these experiments is not directly measured, though it can be estimated from force-time curves. If we assume maximum contact area is maintained at maximum force and contact area of a single digit is lost when the force drops to zero,

the rate of area loss is estimated to $0.89mm^2/s$. We can convert this to a linear rate by taking the square root to estimate a crack velocity of $30mm/s$. For the normal tack experiments, the rate of crack propagation is directly measured to be $0.2mm/s$. Previous research describes the dependence of G on the crack velocity to the n power (i.e., $G \sim V^n$), where n is an empirical constant reported to be between 0.5 and 0.7 for elastomers [16]. If we compare G in shear to G in the normal direction, using n=0.6, the G in shear is estimated to be $\sim$20 times larger than the G in the normal direction. Considering these three mechanisms of frictional energy dissipation, mode of stress transfer, and rate-dependent adhesion, we expect the G_c in the shear direction to be larger than the G_c measured in the normal direction by more than an order of magnitude.

2.7 Conclusions

The adhesive system of the gecko includes a variety of components with varying modulus, stiffness, and geometric arrangement to achieve a design that effectively transfers load from the animal to the adhesive interface. We created a geometric arrangement of adhesive components in a synthetic system, inspired by the foot of the gecko, such that explicit relationships with the compliance and adhesive force capacity of a multiple contact system are developed. We found that the system compliance depends directly on the angular spacing between adhesive digits. Additionally, we found that the adhesive force capacity depends inversely on the angular spacing between adhesive digits. Explicit relationships were developed to quantify the trade-off of adhesive force capacity as angular orientation between digits is increased, leading to a model for gecko locomotion studies. Furthermore, the explicit relationships developed in this study provide a general framework for existing adhesive devices with multiple contact surfaces, where the influence of variation in compliance of individual components on adhesive force capacity is quantified. Finally, the equations developed

here link materials properties and geometry to optimize the performance of adhesive systems with multiple contact surfaces.

2.8 Acknowledgments

M.J. Imburgia would like to thank M.D. Bartlett and D.R. King for their insight and help with experiments and would like to thank M.D. Bartlett and M.R. Ilton for their help with analysis and revisions. M.J. Imburgia and A.J. Crosby would like to thank D.R. Briggs, C.-Y. Kuo, C.A. Gilman and D.J. Irschick for providing helpful images and analysis of natural adhesive systems. M.J. Imburgia and A.J. Crosby also thank the Human Frontiers Science Program (RPG0034/2012) for funding.

CHAPTER 3

COATING COMPLIANCE OF AN ISOLATED CONTACT IN SHEAR

3.1 Introduction

In this study we investigate the shear deformation and reversible adhesion of a rigid flat punch contacting a soft, laterally-extensive elastomer layer. We investigate the scaling of shear compliance, C, with the ratio of contact radius to elastomer layer thickness, or confinement ratio (a/h), through both experiment and finite element analysis. Using a reversible adhesion scaling analysis we also investigate the relationship between the shear adhesion force capacity, F_c, and the confinement ratio using experiments. We find that the shear compliance of this specific geometry and loading condition depends non-linearly and inversely on the confinement of the system. Additionally, we find that the shear adhesion force capacity scales non-linearly with the confinement ratio. These scalings have significant implications for future normal and shear adhesion studies, especially for the fields of bio-inspired adhesion and micro-contact printing.

3.2 Background

3.2.1 Animal locomotion studies

Our study of a rigid punch shearing a thin elastomer coating is motivated by understanding the scaling of reversible adhesion in nature. For adhesive systems that are reversibly removable, such as the adhesive system of the gecko, the maximum force achievable before interfacial failure, known as the force capacity (F_c), is dependent

on three parameters: (i) the critical strain energy release rate, G_c, which is generally related to the specific interfacial chemistries between two surfaces, (ii) the adhesive contact area, A, and (iii) the inverse of compliance of the testing system, $1/C$ [9]. This scaling of $F_c \sim \sqrt{G_c A/C}$ (Equation 1.8) has been shown to be valid for synthetic and natural systems that range several orders of magnitude in size. Based on physical principles, similar to the foundations of Equation 1.8, hypotheses of evolutionary pathways for scaling reversible adhesion in nature have primarily focused on the development of setae, or hairy protuberances on animal attachment pads, which have been proposed to impact G_c [18]. These hairs provide enough flexibility to make adhesive contact with an ecological substrate, while also being stiff when loaded. There are several physical mechanisms that highlight the impact of varying shape and arrangement of synthetic adhesive posts, which mimic the shape and structure of setae, on G_c, including increased adhesive perimeter [18], optimal contact shape [55], and sub-critical attachment size [56]. These studies led to the creation of engineered biomimetic adhesives that have outperformed the abilities of the gecko [57], the largest animal to use reversible adhesion for climbing. However, most of these devices have been limited to sizes less than 1cm^2. Additionally, more recent biological research has highlighted that the shape and arrangement of setae in closely-related animals (geckos, flies, beetles, and spiders) does not change significantly for animals that range more than three orders of magnitude in size [58, 59], leaving open questions as to what other mechanisms explain the scaling of reversible adhesive force with system size.

A recent study by *Gilman et al.* demonstrated that the ratio of A/C was the most significant descriptor of the variation in adhesive force capacity in closely-related organisms (gecko family) that range an order of magnitude in size [25]. This finding implies that larger animals have developed less compliant loading systems to accommodate larger force capacities. To substantiate these findings, we proposed shear

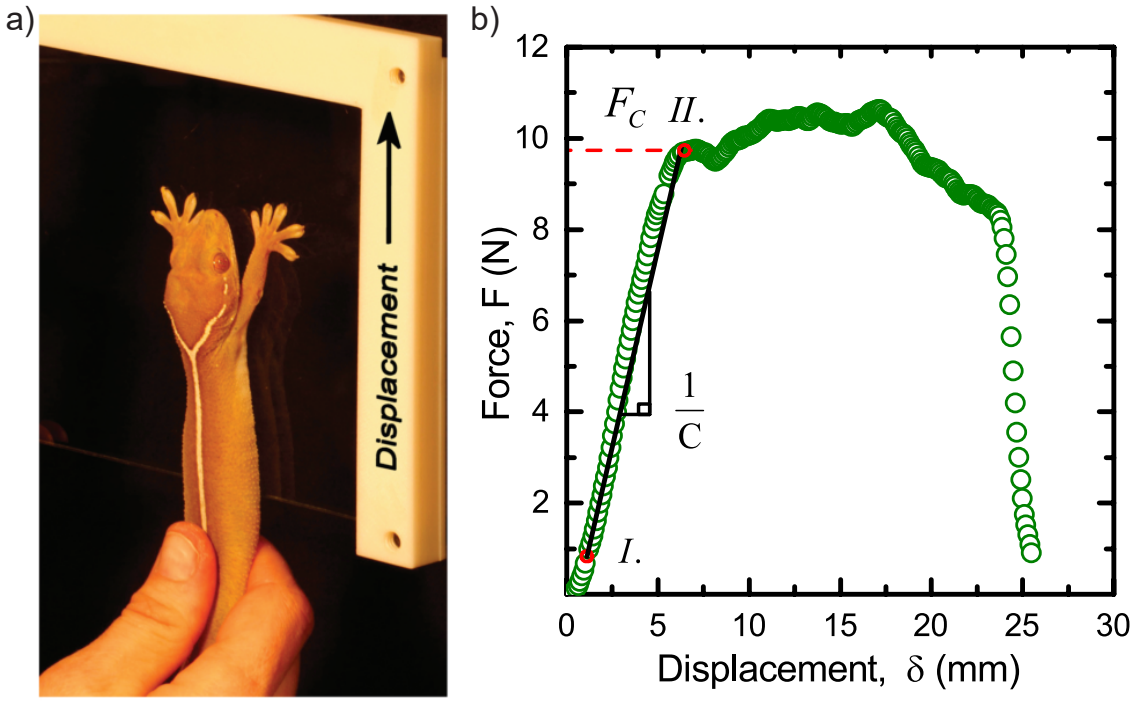

Figure 3.1. Lap adhesion testing of a gecko on glass. a) Image of Gecko testing adapted from Ref [25]. The gecko, gripped by an animal handler at the torso, is encouraged to place its two forelimb feet onto glass. The glass is attached to a force sensor and a displacement actuator. b) Representative force-displacement curve of a gecko adhesion test from Ref [25]. Force capacity, F_c, is the maximum value of adhesive force before slip occurs. Compliance, C, is the inverse of the slope of the load-displacement curve.

adhesion experiments of animals adhering to elastomer substrates, where the compliance of the elastomer substrate is changed systematically via thickness modulation to directly effect the animal's adhesive force capacity. The design of compliant substrates that affect the performance of an animal's adhesive system requires (i) knowledge of the compliance of a animal's adhesive system in a rigid testing setup and (ii) understanding the compliance of a thin elastomer layer sheared by an isolated contact.

The compliance of a gecko's adhesive system has been previously quantified using a lap adhesion testing setup. This setup consists of a rigid substrate attached to a load cell and displacement actuator. While the substrate translates, a gecko, grasped at the torso by the animal handler, is encouraged to place its two front feet onto the

rigid substrate [9, 24, 25, 60] (Figure 3.1a). During the test, when the gecko's adhesive system is in extension, the force exerted on the substrate is measured (Figure 3.1b).

To test the existing theory that compliance is a significant descriptor of the variation in adhesive force capacity for animals that scale in size, we suggest adding an elastomer layer of varying thickness onto the rigid substrate. To design this experiment, it is necessary to know the influence of elastomer layer thickness, relative to the contact area, on the compliance of the system in shear. The deformation of an elastomer layer in shear has been studied for non-confined systems such that the elastomer layer is infinitely thick compared to the size of the contact [61, 62]. Here, we investigate the scaling of shear compliance with the confinement ratio, or the ratio of contact area to elastomer thickness (a/h), in a model testing system and how this scaling will influence the force capacity of the adhesive system. This work will guide future studies on directly influencing the force capacity of animals during lap adhesion testing.

3.2.2 Isolated contact deformation

The case of an isolated contact deforming an elastic coating has been widely studied for the purposes of quantifying materials properties of the elastic coating, such as the elastic modulus and hardness [63], as well as studying the adhesion between the contacting object and elastic coating in the normal [64, 65, 66] and shear [62, 67, 68, 69] directions. Most of these analyses require that the elastic coating thickness is infinite compared to the size of the contacting object or the area of contact, i.e. $a/h \ll 1$. When the elastic coating is relatively thin, the influence of a rigid support substrate becomes more prominent. A thin elastic coating deformed by an isolated contact (Figure 3.2a) is an experimental scenario related to adhesive tapes, rubber tires, contact printing [70], and studying the indentation of human skin [71]. Specifically, this geometry has been studied for describing the tack or adhesion energy between a

rigid punch and an elastic coating [17, 72, 73]. It has been recently shown that the normal adhesive force capacity can be tuned by altering the thickness of the elastic coating with implications for transfer printing of fragile devices [70, 74]. However, the effect of coating materials properties and geometry, as well as punch geometry on adhesion and deformation in shear (Figure 3.2b), has not been extensively studied.

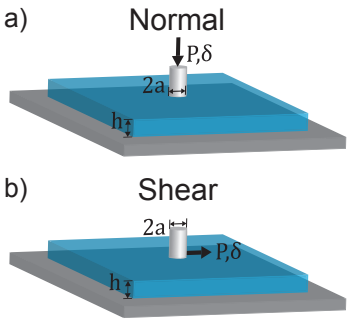

Figure 3.2. Deformation of an elastic coating (blue) by a rigid, axisymmetric punch (light grey) in full-friction contact. a) The normal deformation of a coating. b) The shear deformation of a coating.

3.3 Approach

3.3.1 Shear deformation of a confined system with an isolated contact

Previous studies on shearing a finite thickness elastic coating with a rigid, isolated contact have focused on understanding the scaling of separation stress and the limits at which elastic instabilities occur [75, 76, 77]. Though these previous studies involved experiments and geometries similar to the experiments in our study, an explicit relation for the shear compliance of an isolated contact and coating with parameters such as contact area, coating thickness, and materials modulus has not been developed. Here, we present a comprehensive study on how materials geometry and mechanical properties influence the shear deformation across both confined and non-confined regimes.

To understand the relevant geometric and materials relations for shear compliance of a confined system, we first review the geometric and materials relations for normal

compliance of confined systems developed previously. We focus on a rigid, axisymmetric punch in full-friction contact with a deformable material, where the normal compliance of an incompressible material ($\nu = 0.5$), in the limit that $a/h << 1$, is described as [78]

$$C_n \ (h \to \infty) \equiv C_{n,\infty} = \frac{3}{8aE} \tag{3.1}$$

where $C_{n,\infty}$ is the normal compliance in the infinite thickness limit, a is the radius of contact of the punch, and E is the Young's modulus of the indented material. For finite values of thickness (i.e., $a/h \sim 1$), a semi-empirical relationship has been previously described as [17]

$$C_n = \frac{3}{8aE}\left[1 + 1.33\left(\frac{a}{h}\right) + 1.33\left(\frac{a}{h}\right)^3\right]^{-1} \tag{3.2}$$

where C_n is the normal compliance. For large values of coating thickness, the second and third terms in Equation 3.2 approach zero and the overall expression approaches that of Equation 3.1. For small values of thickness, the second and third terms of Equation 3.2 become more prominent in determining the compliance scaling.

For the same system geometry and assumptions, with the exception of a macroscopic shear applied to the system, we hypothesize the scaling of compliance will follow a similar form to Equation 3.2. For the condition that $a/h << 1$ and the coating is incompressible, the shear compliance of an isolated contact scales as [61]

$$C_{s,\infty} = \frac{3}{16a\mu} \tag{3.3}$$

where $C_{s,\infty}$ is the shear compliance in the infinite thickness limit and μ is the shear modulus of the elastic coating. This relation follows the same scaling as the normal compliance analog (Equation 3.1) and differs by a factor of $\frac{1}{2}E/\mu$. In this work we develop a semi-empirical relation that is the shear compliance analog of Equation 3.2.

3.3.2 Force capacity of a reversible adhesive contact in confinement

In addition to investigating the influence of confinement on coating compliance, we highlight the contributions of the confinement ratio to the scaling of adhesive force capacity for a reversible adhesive contact from confined to non-confined regimes. The three research studies mentioned previously concerning macroscopic shear applied to a confined system focused on qualitative or empirical relations to describe the influence of coating thickness on separation stress [75, 76, 77]. *Barquins et al.* studied the sliding between a hemispherical indenter and a gradient-thickness coating, finding that the size of contact and area of Schallamach wave propagation was qualitatively reduced as coating thickness decreased [75]. *Rand and Crosby* studied the sliding between a hemispherical indenter and an elastic coating with line defects, developing an empirical relation to describe the force required to slide over the line defect relative to a defect-free sample [76]. *Chaudhury and Kim* studied the sliding between a flat rigid probe and an elastic coating, focusing on limits at which interfacial instabilities occurred [77]. To describe the limits of interfacial instabilities for a rigid punch shearing a confined coating, *Chaudhury and Kim* developed scalings of separation stress with geometric and materials parameters such as coating thickness, contact area, work of adhesion, and shear modulus:

$$\sigma_{s,confined} \sim \frac{a}{\ell}\sqrt{\frac{G_c\mu}{h}} \tag{3.4}$$

where $\sigma_{s,confined}$ is the shear stress for adhesive failure dictated by confinement, a is the punch radius, ℓ is the distance above the surface at which shear force is applied, G_c is the critical strain energy release rate between the punch and the film, μ is the shear modulus of the coating, and h is the thickness of the coating, and

$$\sigma_{s,instability} \sim \frac{a^2}{h\ell}\sqrt{\frac{G_c\mu}{h}} \tag{3.5}$$

where $\sigma_{s,instability}$ is the shear stress for adhesive failure dictated by interfacial instabilities. Equation 3.4 describes the pronounced effect of ℓ, a length scale highlighted in Figure 3.3, on a confined system in shear, where a large ℓ in comparison to punch radius, a, results in a significant peel moment. Equation 3.5 incorporates an additional term of a/h to Equation 3.4 to account for the additional strain energy stored due to interfacial instabilities, such as fingering instabilities [79]. Beyond scaling analyses, *Chaudhury and Kim* presented an empirical relation for the influence of ℓ/a on separation stress by fitting Equation 3.5 to experimental data, finding that a larger ℓ/a results in a lower separation stress. Though these studies are useful for determining limits of interfacial instabilities in confined systems under shear loading, an explicit relation for the force capacity in shear as a function of confinement has not been presented previously. Here, we develop a semi-empirical relation for adhesive force capacity of a rigid punch in shear contact with an elastic coating ranging from confined to non-confined regimes. We adapt the reversible adhesion scaling of Equation 1.8 to describe experimental data and develop an explicit relation for adhesive force capacity and confinement using a compliance equation developed from shear deformation experiments.

3.4 Experimental

3.4.1 Lab experiments of punch in shear

A shear displacement is applied to a rigid punch in contact with an elastomer coating on glass using an Instron 5564 universal testing machine. The testing machine is equipped with a fixture to apply lateral force to the punch at a fixed distance from the elastomer surface, ℓ (Figure 3.3). We use six polished steel punches (rms $\sim 100nm$) of radii ranging from 0.75mm-3.8mm [74], and coatings of four different thicknesses ($0.24, 0.77, 1.44$,and 12.5mm). A poly(urethane)(PU) elastomer [F15, BJB Enterprises, Inc.] is used for the coating, where the PU elastomer pre-polymer

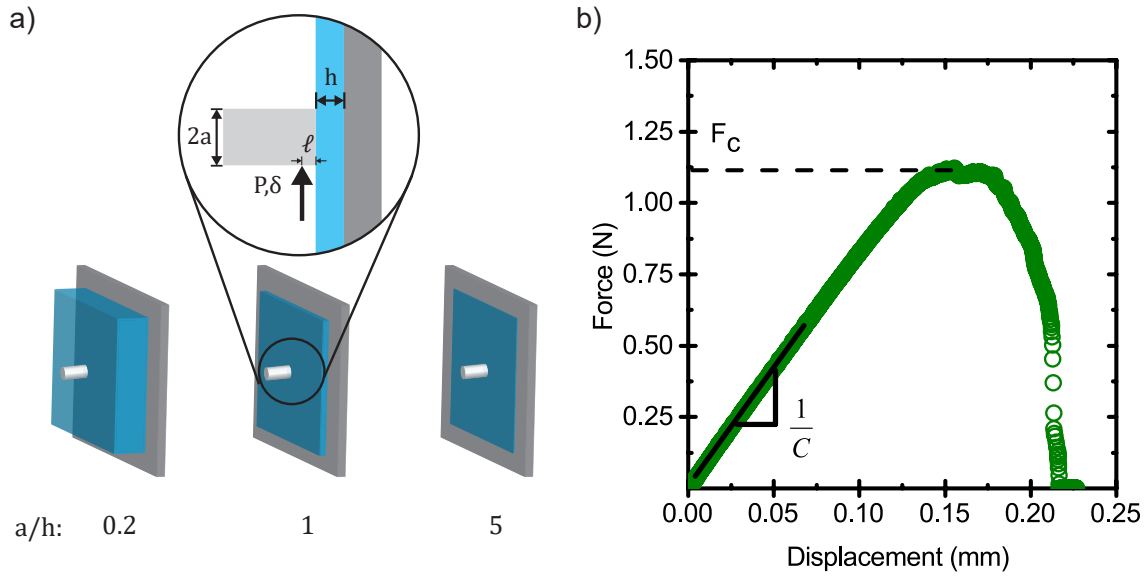

Figure 3.3. Shear deformation and adhesion testing. a) The normal deformation of a coating. b) The shear deformation of a coating.

and cross-linker are mixed according to supplier recommendations (45:100), degassed for 3 min, cast onto plate glass molds using a draw-down process, and cured at 20°C for 24 hrs. Elastomer coatings adhered to glass plates are fixed into the testing setup vertically and punches are pressed into adhesive contact with the elastomer coating. The weight of the punch did generate a moment, but not sufficient as to cause peel. Tests are conducted at a fixed average shear strain rate, $\dot{\gamma} = 10^{-2}$ s^{-1} to minimize variation in G_c due to rate effects. $\dot{\gamma}$ is calculated by normalizing the displacement rate of the testing setup, $\dot{\delta}$, by the elastomer coating thickness, h. A CCD camera [EO-1312C, Edmund Optics] was used to track contact area during loading. Shear force-displacement curves were analyzed for determining the compliance due to shear deformation and the shear adhesive force capacity. The slope of the force-displacement curve corresponds to the inverse of the compliance of the loading system. We measured the slope up until $0.5F_c$ which, in accordance with contact area measurements, corresponds to the earliest point at which an interfacial crack begins to propagate. The force capacity of each experiment is determined by taking the maximum force of

the force-displacement curve, which corresponds to the point of catastrophic adhesive failure.

3.4.2 Elastomer characterization

A shear modulus of $\mu = 94$ kPa (± 3 kPa standard deviation, n=7) and a critical strain energy release rate of $G_c = 0.17 \pm 0.02$ J/m^2 are measured from normal adhesion (tack) tests on independent samples of elastomer prepared under identical curing conditions. Tack tests are conducted using a 4.71mm radius glass hemispherical probe indenting a 3.2mm thick slab of elastomer at a rate of $10\mu m/s$. A custom-built contact adhesion testing setup was used, consisting of a displacement actuator [Inchworm 8300, Burleigh Instruments], a microscope for imaging contact area [Zeiss Axiovert 200M], and a custom-built single capacitor-aluminum cantilever load cell [PISeca D-510.020 single-electrode capacitive sensor and PISeca E-852.10 signal conditioner, Physik Instrumente, GmbH]. Elastomer modulus and critical strain energy release rate are determined using a JKR analysis [16], where G_c corresponds to the value at maximum tensile load. Further detail of this analysis can be found in Section 2.5.2 in Chapter 2 of this dissertation.

3.4.3 Finite-element modeling of punch in shear

We supplement lab experiments with loading, geometry and material equivalent finite element modeling (FEM) using an ABAQUS® 6.13-4 package to analyze the scaling of shear compliance with confinement (Figure 3.4). An analytically rigid disk of radius 1mm was constrained to the nodes on the top surface of an elastic coating, where a tie constraint was placed between the nodes and disk to prevent relative slip. The bottom surface of the elastic coating was designated as rigid and fixed in space. The elastic coating thickness was varied from $0.1 - 10$mm. The lateral dimensions of the elastic coating (xz-plane) were square, fixed at $25mm$ for each side. The mesh was refined based on relative geometries. In the thickness direction

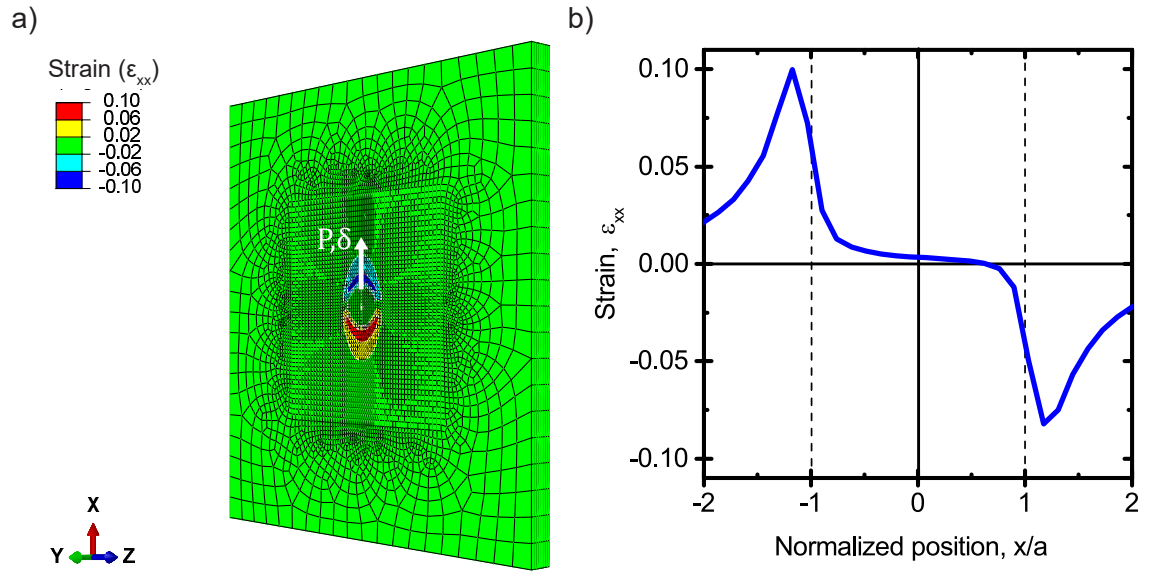

Figure 3.4. Finite-element model of confined shear punch. a) Mesh and x-direction strain field for a/h=1. b) Plot of x-direction strain along the centerline of the punch vs normalized position within the contact region, (x/a).

(y-direction), the mesh size was refined to 10 elements. In the xz-plane, the mesh was split into two regions. The center region spanned 10x10mm and had volumetric elements with xz-planar dimensions of 0.1x0.1mm each. The outer region element sizes and shapes were optimized for conserving simulation time. The element type used for simulations were 8-node, linear, generalized stress elements with reduced integration and hourglass control (C3D8RH). For the constitutive relation of the elastic coating, a neo-Hookean model was used, with a shear modulus of $\mu = 100$ kPa and a Poisson's ratio of $\nu = 0.49$. A fixed average shear strain of $\gamma = 0.1$ is applied to the elastomer such that the displacement applied to the disc is calculated by $\delta = \gamma h$. Simulations consist of 10 sequential steps of 0.1 total strain. Displacement-load data at a reference point on the analytically rigid disk are generated for each confinement scenario. Compliance of each confinement scenario is quantified by applying a linear fit to the load-displacement data and extracting the slope. All linear fits had R^2 values above 0.99.

3.5 Results and discussion

3.5.1 Semi-empirical relation for compliance

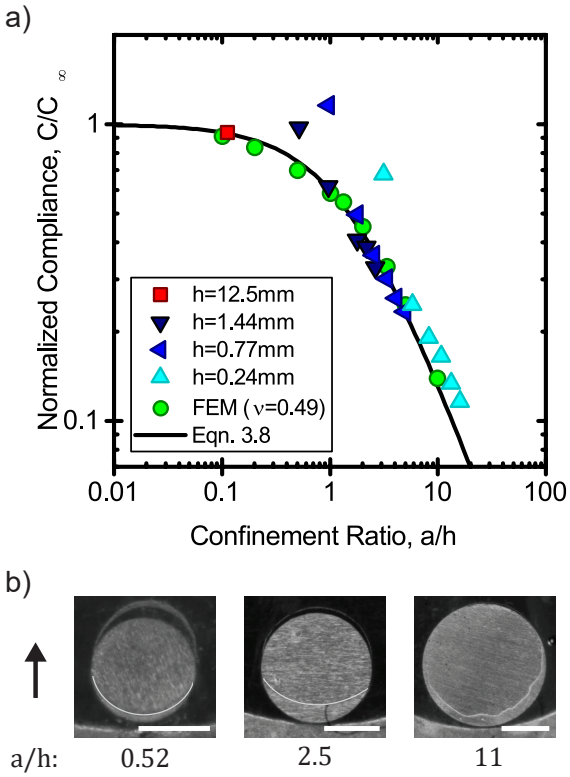

Figure 3.5. Shear compliance scaling and contact area at initial crack propagation. a) Normalized compliance vs. confinement ratio. Normalized compliance is calculated by normalizing measured compliance values by calculated Equation 3.3. Equation 3.8 is represented by the solid black line. b) Contact area images at the onset of crack propagation for three different confinement ratios. White lines are added to the left and center images to enhance the visibility of the contact line. Confinement ratios are noted below each image. The black arrow represents the direction of applied shear displacement. All scale bars are 1mm.

We conduct shear experiments of a flat ended punch on an elastomer coating (Figure 3.5a) to describe the relationship between shear compliance and confinement ratio. For experiments, four elastomer coatings of varying thickness are sheared by six punches of varying radius. The experimental data, represented by the filled triangles and the filled square, generally appear to collapse onto a single curve. To explicitly describe the effect of the confinement ratio on shear compliance, we supplemented lab

experiments with FEM, represented by the filled green circles. The FEM and experimental data follow a similar scaling over the confinement values tested, justifying the use of FEM for fitting a semi-empirical relation. In general, the compliance scaling of an isolated shear contact can be described as

$$C = C_\infty \, f\left(\frac{a}{h}\right) \tag{3.6}$$

where C_∞ is the compliance of a coating with infinite thickness (Equation 3.3) and $f(a/h)$ is a function that describes the influence of confinement, or the ratio of (a/h), on the compliance. Based on a normal compliance analog [17], we fit a polynomial function to the FEM data to describe the influence of (a/h)

$$f = \left[1 + \alpha(a/h)^1 + O(\beta_n(a/h)^n)\right]^{-1} \tag{3.7}$$

where O represents higher order polynomial terms. We find that only $(a/h)^1$ describes the data for thinner coatings, with a coefficient of 2/3 and $R^2 = 0.93$. The final relation becomes

$$C = \frac{3}{16a\mu}\left[1 + \frac{2}{3}\left(\frac{a}{h}\right)\right]^{-1} \tag{3.8}$$

The experimental data generally follow the semi-empirical relation of Equation 3.8, with the exception of the three outliers with higher than predicted compliances. The $(a/h)^1$ term in Equation 3.8 represents a basic shear block relation. The stress state in the elastomer presented in these experiments involves the compression of material in front of the punch, the extension of material behind the punch, and the shearing of a cylinder of material below the punch. The unity term of Equation 3.8 describes the shearing of elastomer in the infinite thickness limit, which is related to the extension of material behind the punch and compression of material in front of the punch. For

a confined system, if the volume of material directly below the punch is approximated as $V = \pi a^2 h$, the compliance of a cylinder of elastomer of volume, V, sheared between two rigid plates is described as $C = h/(\pi a^2 \mu)$ - a similar relation expressed by the $(a/h)^1$ term in Equation 3.8.

The three outlying data points with significantly higher compliances are collected using the smallest punch radius of $a = 0.75$mm. We attribute the larger values of compliance measured to a large peel moment applied to the punch. Evidence for this is shown in Figure 3.5b for the left image with a confinement ratio of 0.52. At the bottom of the image, a peel front is beginning to advance across the sample and the elastomer is in tension. At the top of the image, a pronounced curvature is present. We attribute this curvature to interference arising from a local indentation of the elastomer surface. For the smallest punch ($a = 0.75$mm), the height above the sample at which force is being applied, ℓ, is similar to the radius of the punch ($\ell/a = 0.4$). As described previously by *Chaudhury and Kim*, a significant moment is applied to the sample, leading to failure dominated by peel [77].

3.5.2 Adhesive force capacity vs. Confinement

The results of force capacity from the experiments are shown in Figure 3.6. We plot experimentally measured values of F_c and A/C in Figure 3.6a to show the scaling of our measurements in accordance with Equation 1.8. The data from experiment appear to collapse onto a single line, with the exception of a few outliers for small values of A/C. The outliers at low values of A/C correspond to data of the smallest punch, $a = 0.75$mm. This adhesive failure, as shown in the left image of Figure 3.5b, exhibits larger compliance values before contact area reduction and is dominated by peel failure. As described in the Approach section above, *Chaudhury and Kim* previously showed that an increase in ℓ/a would lead to a reduction separation stress [77].

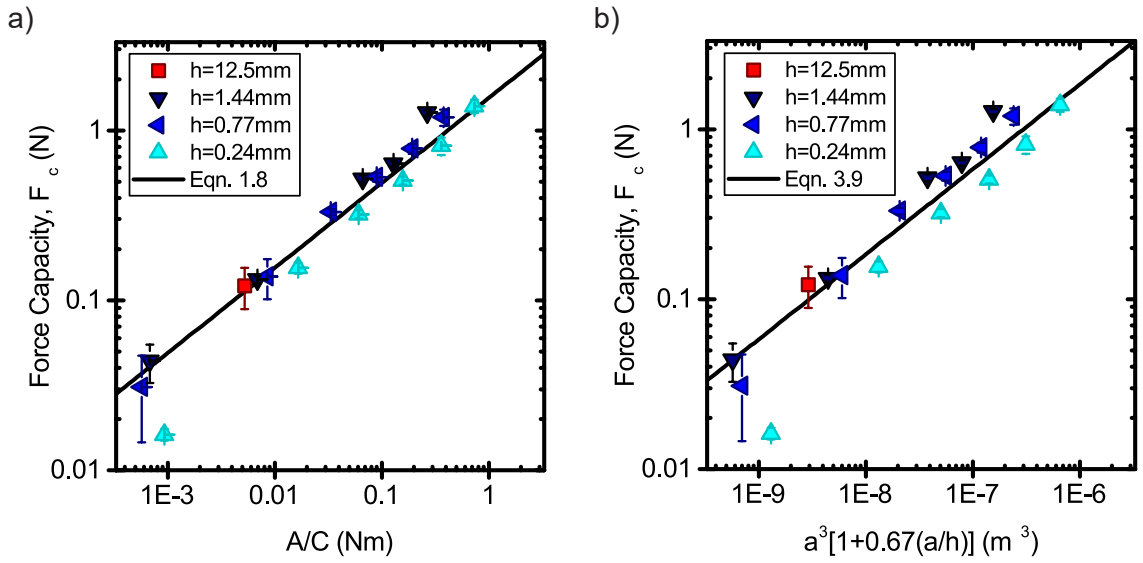

Figure 3.6. Force capacity of a confined shear punch. a) Force capacity vs. A/C. Equation 1.8, represented by the solid line, is fit to the data by a single parameter, $G_c = 1.5$ J/m^2. b) Plot of Force capacity vs. confinement. Equation 3.9, represented by the solid line, is fit to the data by a single parameter of $G_c\mu$=100 J/m^2 kPa.

The solid black line in Figure 3.6a represents Equation 1.8, where the slope was fit by a single parameter of $G_c = 1.5$ J/m^2. We note that this G_c value represents the critical strain energy release rate of this specific PU elastomer under shear loading, nearly an order of magnitude larger than the G_c values of the same PU elastomer under normal loading during tack tests ($G_c = 0.16$ J/m^2). The magnitude of G_c in shear as compared to G_c in the normal direction is expected to be larger due to several factors, including energy dissipation from friction or surface instabilities [53, 77, 80] and rate of crack propagation [54].

To emphasize the existence of different mechanisms of adhesive failure in these experiments, we draw focus towards results shown in Figure 3.5b, where contact area images at the onset of adhesive failure provide a qualitative perspective. The left image, as discussed previously, indicated pronounced peel failure. The center image, with a confinement ratio of 2.5, has a smooth contact line with a slightly noticeable curvature at the top due to local indentation, indicative of both shear and peel

failure. The right image, with a confinement ratio of 11, shows the presence of an undulating contact line at the bottom of the image, indicative of a fingering instability. Additionally, Schallamach waves have been observed during adhesive failure for samples with confinements on the order of ~ 1. It is probable that additional energy is dissipated due to the presence of these instabilities, as suggested in previous experiments [77], increasing the measured value of G_c compared to that measured by normal tack experiments. The presence of "microslip" has also been shown previously to exist experimentally in shear loaded geometries, even when relative sliding between the rigid contact and the elastomer is not observed macroscopically, leading to additional energy dissipation [53]. Additionally, the rate dependence of elastomer adhesion can also play a significant role in augmenting the measured G_c. When measuring the G_c of the elastomer in the normal direction, a maximum crack velocity of $200\mu m/s$ is observed. During these shear experiments, an approximate crack velocity of $100\mu m/s$ is observed. With these observations in mind, we do not expect rate dependent adhesion to significantly contribute to the larger value of G_c observed in shear compared to the normal direction. We acknowledge the presence of interfacial instabilities in some of our experiments, characterized by undulating crack fronts, and the possibility for microslip to be present. However, for the purposes of explaining the scaling of shear adhesive failure over orders of magnitude in size from confined to non-confined, the effect of interfacial instabilities on adhesive force capacity are captured by our fitting parameter, G_c.

The reversible adhesion scaling of Equation 1.8 is a general relation for any reversible adhesive system - independent of system geometry or specific loading conditions. To utilize Equation 1.8, one needs to directly measure the compliance of the loading system. The scaling of adhesive force capacity can be described in terms of the materials properties and degree of confinement by substituting Equation 3.8 into Equation 1.8.

$$F_c = \sqrt{\frac{32}{3}\pi G_c \mu}\sqrt{a^3\left[1+\frac{2}{3}\left(\frac{a}{h}\right)\right]} \tag{3.9}$$

According to Equation 3.9, if the thickness of the coating is reduced, F_c of the adhesive system increases; if the size of the contacting object is reduced, F_c of the adhesive system decreases. Figure 3.6b represents the experimental data in such a way that the relationship between F_c and confinement is highlighted. Equation 3.9 is fit to the data by a single parameter of $G_c\mu$=100 J/m^2 kPa. This fitted value is in general agreement with the experimentally measured shear modulus, μ = 93 kPa and the experimentally fit value of $G_c = 1.5$ J/m^2.

3.6 Conclusions

Studying the deformation of a thin elastic coating in shear is relevant for numerous applications, including rubber tire friction, skin adhesion and friction, contact printing, and reversible adhesives. In this study we investigated the shear deformation and reversible adhesion of a rigid flat punch contacting a soft elastomer layer for the purposes of explaining reversible adhesion. We developed a scaling for shear compliance with the confinement ratio through both experiment and finite element analysis. Using a reversible adhesion scaling analysis we also probed the relationship between the shear adhesion force capacity and the confinement ratio using experiments. We found that the shear compliance of this specific geometry and loading condition depends non-linearly and inversely on the confinement of the system. Additionally, we found that the shear adhesion force capacity scales non-linearly with the confinement ratio. For this specific loading geometry we highlighted sources of interfacial energy dissipation that lead to measured values of adhesion energy release rate much higher than anticipated. The significance of this work lies in the explicit equations that relate system geometry and loading to a predictable compliance and reversible adhesive force capacity. These measurements and equations have notewor-

thy implications for future normal and shear adhesion studies, especially for the fields of bio-inspired adhesion and micro-contact printing.

3.7 Acknowledgments

M.J. Imburgia would like to thank M.D. Bartlett and J.T. Pham for their insight and help with experiments and would like to thank M.D. Bartlett for his help with analysis and revisions. M.J. Imburgia and A.J. Crosby would like to thank C.A. Gilman and D.J. Irschick for providing helpful discussion and analysis of natural adhesive systems. M.J. Imburgia and A.J. Crosby also thank the Human Frontiers Science Program (RPG0034/2012) for funding.

CHAPTER 4

ROLLING WRINKLES ON ELASTIC SUBSTRATES

4.1 Introduction

We present and develop a patterning technique that relies on the contact mechanics and geometry of rolling to create mechanically tunable wrinkled surface structures. A plate-to-roll (P2R) geometry was used to laminate a thin film onto a soft substrate. First, a soft substrate is draped around a roller and pressed into contact with a thin film supported on a plate. Once the plate begins to translate, the thin film preferentially laminates onto the soft substrate. During this process the deformation of the soft substrate due to contact load, as well as deformation due to bending around the roller, can induce wrinkling. Importantly, we demonstrate that the amplitude of wrinkles can be controlled by applied contact load and roller curvature. We demonstrate this using a 150nm poly(styrene) thin film supported on a silicon wafer and a 2mm thick poly(dimethyl siloxane) rubber substrate. Wrinkle feature size consists of amplitudes of $0.2 - 4\mu m$ and wavelengths of $15 - 20\mu m$. We develop semi-empirical equations to describe the effect of applied contact load and roller curvature on the wrinkle aspect ratio. To support experimental relationships between contact conditions and strain at the roll/plate interface, finite element modeling (FEM) of a soft substrate in full-friction rolling contact with a rigid plate is conducted.

4.2 Background

4.2.1 Motivation

There have been numerous proposed applications that utilize surface wrinkling as a patterning technique, including diffraction gratings [27, 81, 82], optoelectronics [83, 84], stretchable electronics [85, 86, 87, 88, 89, 90], microlens arrays [91, 92, 93], responsive windows [5, 93], tunable adhesives [94, 95, 96, 97, 98], wetting and antifouling surfaces [5, 99, 100, 101, 102, 103], microfluidics [93, 104, 105, 106], particle sorting [107, 108], cell growth and motility [109, 110, 111, 112, 113, 114], and material metrology [115, 116, 117, 118, 119, 120, 121]. However, the production of surface wrinkles with controlled order and micron scale dimensions in a scalable manufacturing process is challenging. To address these challenges, we demonstrate a robust method to create surface wrinkles using the contact mechanics of rolling, which could prove quite useful in the development of a roll-to-roll (R2R) surface wrinkling manufacturing process.

Previous studies have utilized a similar rolling technique for transfer printing of fragile devices [122, 123], as well as for fabricating wrinkled membranes [124]. However, these studies do not assess the capability to actively control the aspect ratio, the ratio of amplitude to wavelength, of surface wrinkles - a necessity for the realization of the proposed applications that utilize the wrinkling instability [35]. Here, we control both the aspect ratio and periodicity of surface wrinkles by adjusting applied strains through applied normal load and roller radius. A numerical contact mechanics model is developed using materials properties and geometric parameters to confirm results from lab-based experiments.

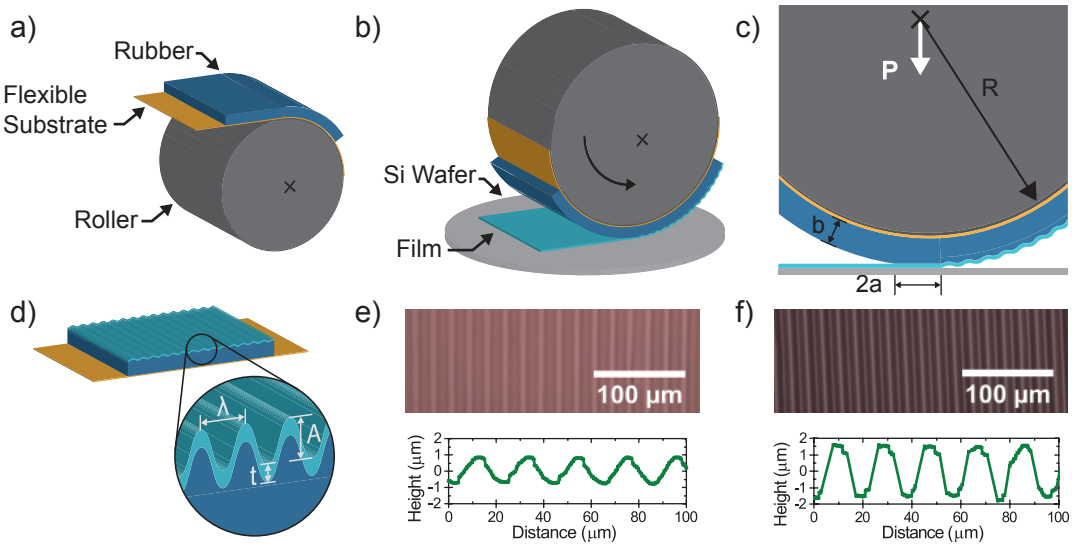

Figure 4.1. Schematic of the plate-to-roll (P2R) process. a) A rubber-like layer attached to a flexible substrate, or web, is wrapped around a roller. b) The roller with the rubber-like layer and web is pressed into contact with a thin, rigid film supported by a silicon (Si) wafer. The thin film is transferred from the Si wafer to the rubber-like layer in this plate-to-roll (P2R) technique. c) During the film transfer process, several parameters such as contact load per unit width, P, roller radius, R, rubber-like layer thickness, b, and contact width, 2a, are considered. Once contact is released, the thin film wrinkles. d) When the final film/rubber/web composite is released from the roller, a wrinkled surface with a larger amplitude emerges. Peak-to-peak distance, wavelength (λ), peak-to-valley distance, amplitude (A), and film thickness (t) are highlighted in the expanded schematic of the wrinkled surface. e) An optical micrograph of a wrinkled surface after rolling, b)-c). The plot is a line profile along the scale bar, quantified using optical profilometry. f) An optical micrograph of a wrinkled surface after d). The plot is a line profile along the scale bar, quantified using optical profilometry. There is a clear increase in amplitude between the line profiles of e) and f). Figure reproduced with permission from Ref [125].

4.3 Approach

4.3.1 Wrinkling process

We propose a wrinkling method that utilizes a plate-to-roll (P2R) geometry, consisting of a free-rolling cylinder, a flexible inextensible substrate coated with a rubber-like layer, a translating plate with a releasable thin film, and the actuation of force when the rubber-like coating and plate come into contact (Figure 4.1a-c). In the proposed P2R geometry, the compressive strain on the film can be created from either

contact deformation of the rubber-like coating and plate during the rolling process or draping the rubber-like coating around the curved roller surface. Figure 4.1 highlights the P2R transfer process. Figure 4.1e shows evidence of a wrinkled surface while the composite is on the roller, formed due to contact deformation ($\varepsilon_{contact}$). Figure 4.1f shows an increase in wrinkle amplitude due to the imposition of bending strains ($\varepsilon_{bending}$). By tuning the contact load, roller curvature, as well as other properties such as the thin film modulus and thickness, and the rubber-like coating modulus and thickness, a desired wrinkle aspect ratio can be achieved.

4.3.2 Rolling contact

The geometry of contacting rubber-coated rollers is common in the textile, paper, and printing industries. This has led to many studies that specifically describe deformations and tractions at the contact interface for the prevention of wear or failure of manufacturing machines and products [126, 127, 128, 129, 130]. Rolling creep was one of the first unexpected phenomena involving the rolling contact between a rigid roller and a deformable elastic layer [131]. Rolling creep is a difference in peripheral velocity of two contacting surfaces, arising from a difference in tangential strain between the two surfaces [132]. In our experiments (P2R process) the development of tangential strain is the primary mechanism for how wrinkles develop.

Of these previous works, Bentall and Johnson developed a series of models that articulate the effect of normal roller deformation, materials properties, and geometry on the tangential strains that develop between a rigid body and a deformable body during rolling [126]. Specifically, they consider the tangential strain that develops from the contact of an incompressible elastic layer of a finite thickness, which we define as b. In the thin layer limit, where b is much less than the half contact width, a, Bentall and Johnson's relationship between the tangential strain, ε_{xx}, and applied load, geometry, and materials properties can be presented as:

$$\varepsilon_{contact,\ xx} = C_1 \left(\frac{P}{\overline{E}_s\ b}\right)^{n} \left(\frac{b}{R}\right)^{m} \tag{4.1}$$

where P is the applied load per unit width, $\overline{E}_s$ is the plane strain modulus of the elastic layer, R is the radius of curvature of the roller, b is the elastic layer thickness, and C_1, n, and m are constants determined from experimental results. Note that we have arranged Bentall and Johnson's relationship such that the relationship depends on two dimensionless groups, which will guide the analysis of results presented below. In the thin layer limit, $n = 0.4$ and $m = 0.6$, as presented by Bentall and Johnson. The coefficient, C_1, is 0.87 for the full-friction case, and 0.66 for frictionless contact conditions.

4.4 Experimental

4.4.1 Materials and instrumentation

For the rubber-like layer, Sylgard® 184 (Dow Corning), based on cross-linked poly(dimethyl siloxane) (PDMS), was prepared in a pre-polymer:cross-linker ratio of 30:1. Uncured PDMS liquid samples were degassed, poured into a mold, then cured in an oven at 70°C for 6 hours. These conditions provide a cross-linked silicone rubber with an elastic modulus, E_s, of 250 kPa, quantified by contact mechanical tests with a 0.75 mm diameter cylindrical probe of polished steel [94]. We consider the silicone rubber to be incompressible with a substrate Poisson's ratio, ν_s, of 0.5. The thin film was a 170 kg/mol, 2.1 PDI poly(styrene) (PS) (Sigma Aldrich) spun coat from a 3 wt% polymer solution in toluene (Fisher Scientific). Here, we use a PS film modulus, E_f, of 3.3 GPa and a film Poisson's ratio, ν_f, of 0.33 [133]. Flexible substrates used were a $25\mu m$ thick polyimide film (Dupont) and an $80\mu m$ thick adhesive-backed PET tape (3M). P2R process consists of a linear stage (Parker Daedal 104XR) moving the Si wafer laterally and a 3D-printed roller (uPrint SE Plus) able to axially rotate and freely fall in t-slotted aluminum framing (Figure 4.2). Plate translation speed was set

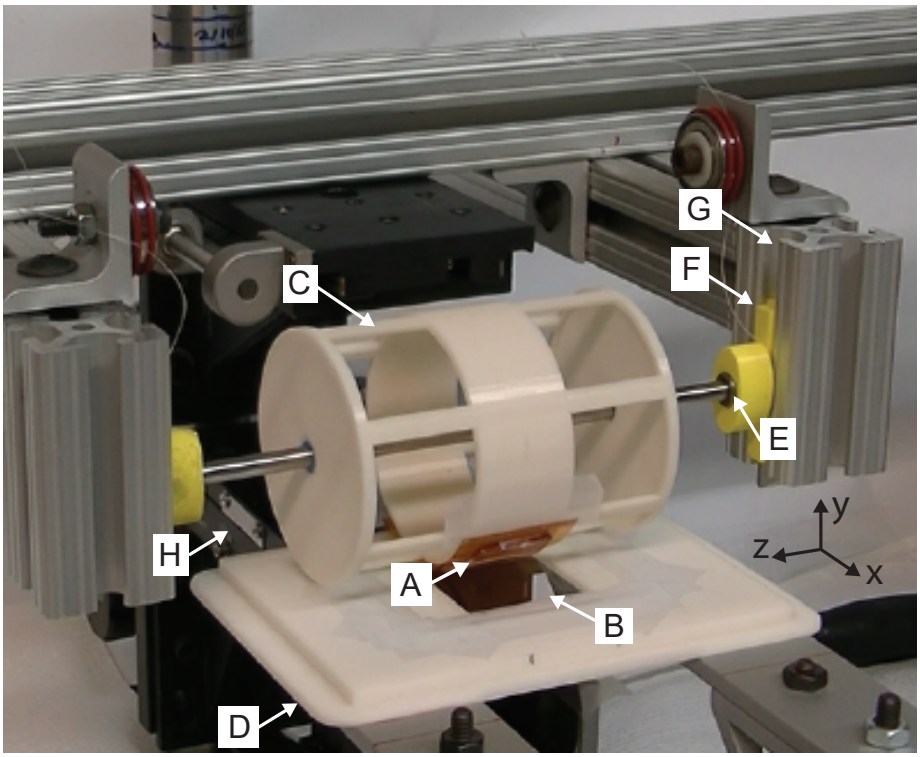

Figure 4.2. Image of custom-built P2R setup. A) PDMS elastomer layer. B) Thin film supported by a rigid substrate (in this image, PS on glass). C) 3D-printed roller. D) 3D-printed translation plate, supporting rigid substrate, driven by linear actuator. E) Linear actuator (Parker-Daedal 104XR) which allows for controlled motion in the x-direction. F) Steel needle-bearings which allow for free rotation about the z-direction. G) 3D-printed rail guide (yellow). H) T-slotted aluminum rail (80/20 Inc.). G) and H) allow for free translation in the y-direction.

at 1 mm/s. Weights were added to the freely-falling roller to increase the amount of normal load applied at the transfer interface. P2R process was conducted in greater than 60% relative humidity to promote transfer of PS film from the Si wafer to the silicone rubber. A Zygo NewView 7300 (Zygo Corp.) optical profilometer was used to quantify the topography of the wrinkled surfaces. Thin film thickness was measured using a Gaertner Stokes Ellipsometer LSE (Gaertner Sci. Corp.).

4.5 Results and discussion

4.5.1 Applied load

To understand the impact of normal load on the formation of surface wrinkles in the P2R geometry, we first conducted a set of experiments where the applied load was varied from 15 N/m to 275 N/m, while all other parameters (R, b, $\overline{E}_f$, $\overline{E}_s$) remained fixed. Figure 4.3a shows the measured values of wrinkle wavelength and amplitude, as observed on the roller prior to release, for these experiments. We observe that the wrinkle wavelength remains nearly constant, while the wrinkle amplitude increases as a function of applied load. We use Equations 1.9-1.11 to determine the applied compressive strain, ε_{xx}, which led to the development of the wrinkles, using measured values of amplitude and wavelength (Figure 4.3b).

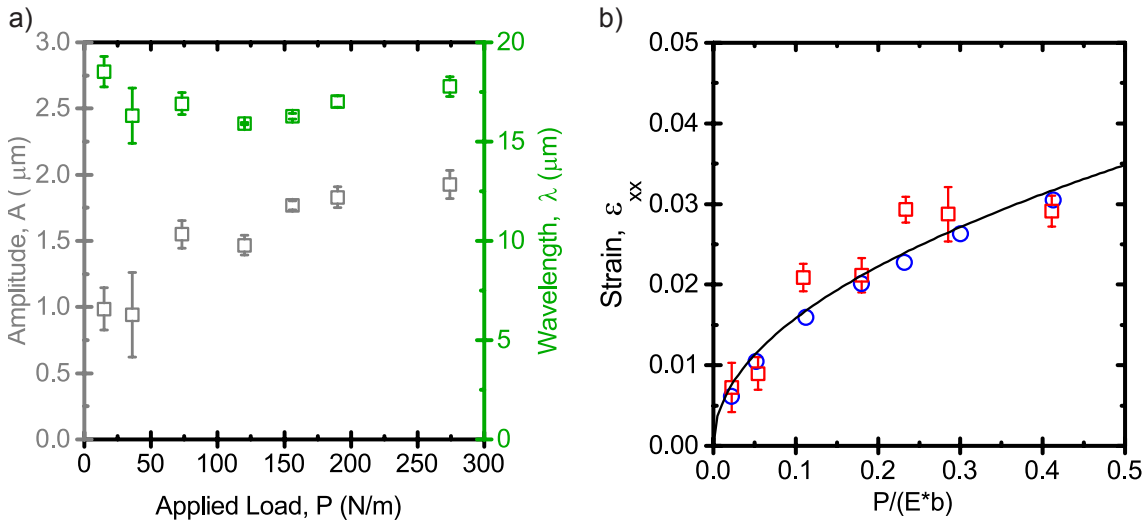

Figure 4.3. Wrinkled structures influenced by applied normal contact load. The influence of normal contact load on strain is represented by the dimensionless group P*(E/R), where E represents $\overline{E}_s$. a) Amplitude (open grey squares) and wavelength (open green squares) of wrinkled surfaces created by various applied contact loads. b) Compressive strain imposed by contact load (open red squares) from wrinkling experiments. Strain in the contact region extracted from FEM (open blue circles). A power law fit (solid line) is applied to both the FEM and experimental data by an exponent, n, and a trivial constant. Figure reproduced with permission from Ref [125].

Following the framework presented in Equation 4.2, we fit the experimentally determined strain values as a function of P/Eb, to determine that $n = 0.49$ for our conditions. This difference in scaling from Bentall and Johnson, who proposed $n = 0.4$, is associated with the difference in the thickness limits. In our experiments, the compliant substrate thickness (2mm) is comparable to the half contact width (1.3mm-3.3mm).

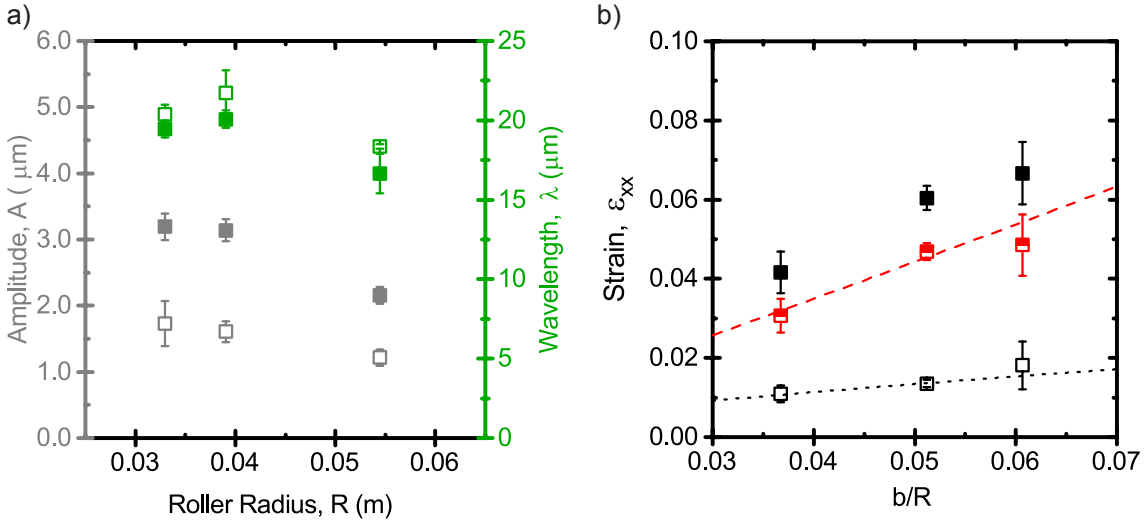

Figure 4.4. Wrinkled structures influenced by roller radius. The influence of roller radius on strain is represented by dimensionless group b/R. a) Amplitude (grey squares) and wavelength (green squares) of wrinkled surfaces created by various roller radii measured after the contact transfer step (open squares) and after removal from the curved surface (solid squares). b) $\varepsilon_{bending}$ (half-open red squares) is calculated from the difference of ε_{total} (solid black squares) and $\varepsilon_{contact}$ (open black squares). A power law fit (black dotted line) is applied to the $\varepsilon_{contact}$ data by an exponent, m, and a trivial constant. Equation 4.2 (red dashed line) is fit to the $\varepsilon_{bending}$ data by a constant C_2. Figure reproduced with permission from Ref [125].

4.5.2 Roller radius

In addition to the applied normal load, the roller radius can play an important role in determining the wrinkle geometry. Roller radius can impact the strain applied to the film/rubber interface in two ways. First, as described by Equation 4.1, the lateral strain of contact is inversely proportional to the roller radius. Second, upon

release of the rubber from the roller, a compressive strain associated with the bending of the rubber layer around the roller is applied to the film/rubber interface. To demonstrate these contributions to the wrinkling strain, we conducted a series of experiments where the roller radius was varied from from 33 mm to 54 mm, while all other relevant parameters remained fixed. We observe that the wrinkle wavelength remains nearly constant, while the wrinkle amplitude decreases as a function of roller radius (Figure 4.4a). These quantities are measured after contact deformation and lamination ($\varepsilon_{contact}$), and additionally after removal from the curved roller surface (ε_{total}).

Following the framework of Equation 4.1, we fit the experimentally determined strain values as a function of b/R, to determine that $m = 0.74$ for our conditions, which is different than the scaling value of Bentall and Johnson ($m = 0.6$). Again, this difference is associated with the finite thickness of the elastic layer in our experiments. We note that for the scaling value found in Figure 4.3b ($n = 0.49$), the data spans over an order of magnitude, justifying a scaling analysis. However, the scaling found here in Figure 4.4b ($m = 0.74$) spans less than an order of magnitude, which is a limitation based on our experimental design. Using the fitted values of n and m, Equation 4.1 is fit to the experimental and FEM data presented in Figure 4.3b to determine $C_1 = 0.42$.

The contribution of bending strain to the P2R process ($\varepsilon_{bending}$) is calculated from the difference between ε_{total} and $\varepsilon_{contact}$. Assuming a neutral bending axis at the interface between the web and silicone rubber layer, an analytical model for the strain due to bending is assumed to be simply

$$\varepsilon_{bending} = C_2 \, \frac{b}{R} \tag{4.2}$$

where C_2 is a fitted constant determined to be 0.90 from the data in Figure 4.4b.

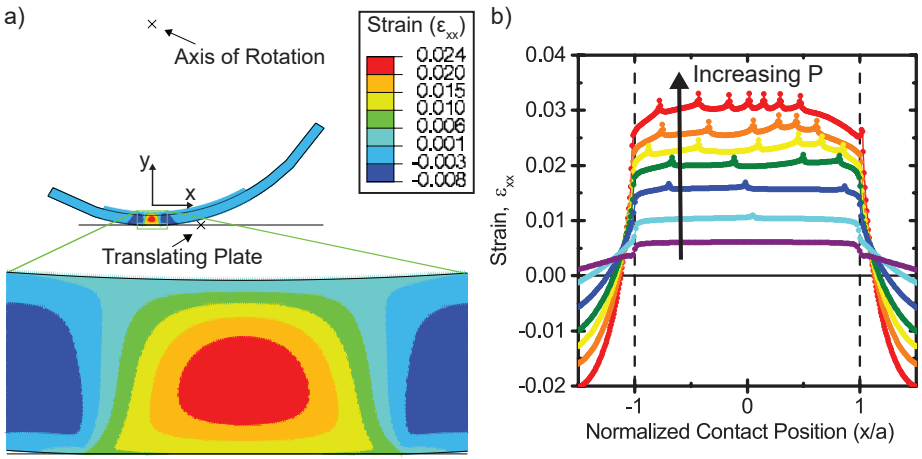

Figure 4.5. Finite Element Model (FEM) data. a) A simulation image (mesh removed) of the FEM model. The scale represents the x-direction strain of each node, where positive values correspond to tensile strain. b) The local x-direction strain for each node, as well as position normalized by the total contact width is plotted for each simulation experiment with a defined applied contact load. Increasing applied loads correspond to increasing values of average strain in the contact region. Figure reproduced with permission from Ref [125].

4.5.3 Finite element model

To provide insight into how the materials properties and geometry control the applied wrinkling strain during the P2R process, we developed a numerical, finite element model (FEM). Two-dimensional finite element simulations were performed using ABAQUS® (Dassault Systemes) software. A neo-Hookean constitutive model was used to represent the stress-strain behavior of the silicone rubber layer. Elements used for simulations were 4-node, bilinear, plane strain elements with reduced integration and hourglass control (CPE4RH). A friction-based contact criterion was implemented using a friction coefficient based on the Amonton-Coulomb law of friction [132]. The friction force between a surface node on the silicone rubber layer and a rigid plane is proportional to the normal force on the node by a value of $\mu = 1.2$. This value was used based on an empirical study to assure that no slip occurs while nodes are in contact, which is consistent with our experimental observation for the

current materials system. The strain values taken from FEM are averaged from the entire contact region (Figure 4.5b). For lower loads, it is evident that the strain is relatively constant throughout the contact region. This trend was previously predicted for the case of an incompressible rubber-like material and a full-friction ($\mu = \infty$) contact condition [126]. For higher loads, there are noticeable fluctuations in the data throughout the contact region. These fluctuations can be explained as an artifact of the simulation conditions that originates from a history of strain at the edges of contact during the initial normal loading. Further explanation of the fluctuations can be found in the following section. Plotting the average strain in the contact region, we find good agreement with our measured strains from the rolling wrinkling experiments. Furthermore, when we fit the first dimensionless group from Equation 4.1 to the FEM data, we find a scaling of $n = 0.49$, concurrent with the scaling found in the wrinkling experiments.

4.5.3.1 Boundary conditions and loading

The general shape of the FEM model is shown in Figure 4.6. The top nodes of the rubber-like layer were tied together (relative motion between two tied entities is restricted) and designated as rigid (no relative translation or rotation allowed) to simulate a rigid roller surface. These nodes were then tied to the axis of rotation. Load is applied to the axis of rotation and the axis of rotation can freely displace in the y-direction. The load on the pin is then transferred and distributed through the rubber-like layer to the contact interface between the rubber-like layer and an analytically rigid plate fixed in space. An increase in load will result in an increase in contact area between the rubber-like layer and the rigid plate. While the load is held at a fixed value, the plate is then translated in the x-direction, inducing a rotation of the rubber-like layer about the pin. Mesh size was set to 25 μm in the contact zone and gradually coarsened to 1 mm at the left and right edges of the geometry. Through

the thickness, the mesh was gradually increased from 25 μm to 500 μm. There was a friction coefficient of $\mu = 1.2$ applied to the contact between the rubber-like layer and the flat rigid surface.

4.5.3.2 Fluctuations due to contact conditions

Because there exists a full-friction contact condition, when the roller is initially loaded, the silicone rubber layer deforms to make contact with the plane without slipping. This results in a parabolic distribution of tangential strain in the contact region, where the center of contact is in a state of compression and the edges of contact are in a state of tension. As the initial normal applied load increases, the magnitude of the tensile strain at the edges of contact increases. Once the plane begins to translate, rolling initiates and the tensile strain at the adhering edge of contact translates through the contact region and eventually reaches the releasing edge of contact. This process occurs once the plane translates a distance on the order of the initial contact width and the system reaches a steady-state.

However, our FEM involves discrete-sized elements and nodes, where contact is defined as a node on a deformable body within a certain distance of a point on a rigid body. In order for a node to come out of contact with the rigid body the normal force at the node must go to zero. In order for a node to make contact with the rigid body the distance between the node and rigid body must be under a threshold value - in this case the default value is 10 nm. For this simulation of rolling contact, nodes at the releasing edge of contact will release a large magnitude of tensile strain and a discrete amount of contact width will be lost. When the distance between a node at the adhering edge of contact and the rigid plane falls below the threshold value, the element must stretch to maintain an appropriate pressure-area relationship based on the elasticity of the silicone rubber layer. This implies that as element size or plate step distance is refined, these fluctuations should dissipate. For this set

of experiments, the minimum element size was 25μm and the minimum plate step distance was 50μm. These values were the lowest achievable while maintaining a reasonable simulation time ($\sim$ 1 hour).

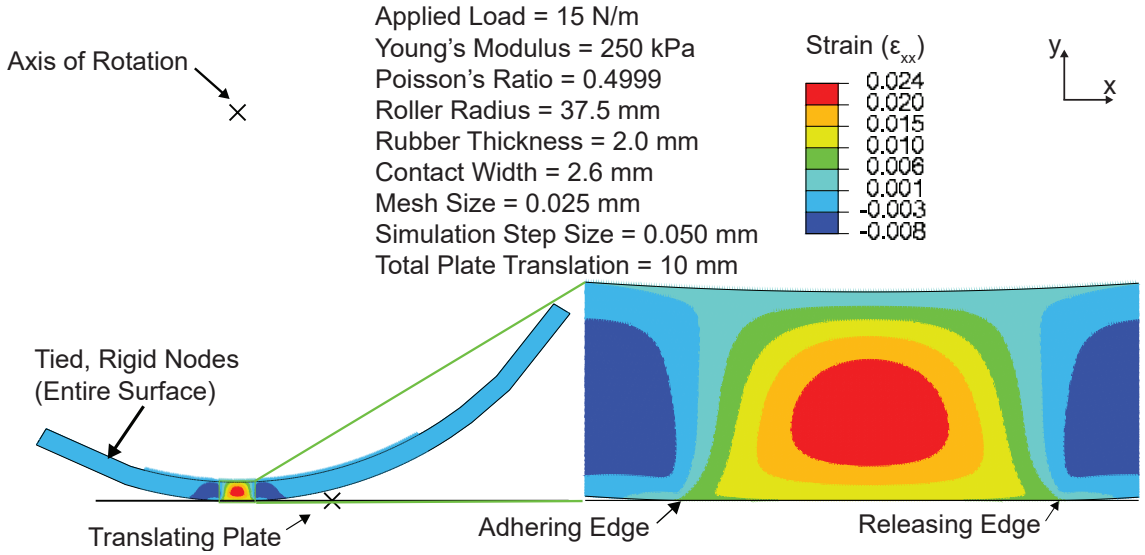

Figure 4.6. Schematic and input parameters of FEM geometry for an applied load of 15 N/m. Figure reproduced with permission from Ref [125].

4.5.4 Controlling wrinkle aspect ratio

Using the semi-empirical scaling relations determined above and the insight provided by the FEM analysis, we develop a comprehensive set of relations that allows the process parameters to be quantitatively related to the aspect ratio of the wrinkles formed by rolling contact. In general, the aspect ratio of surface wrinkles can be defined using Equation 1.9 and Equation 1.11 as

$$\frac{A}{\lambda} = \frac{2t}{\lambda}\left(\frac{\varepsilon}{\varepsilon_c} - 1\right)^{1/2} \tag{4.3}$$

where $\frac{A}{\lambda}$ is the aspect ratio. By inserting Equation 4.1 and Equation 4.2 into Equation 4.3, we develop an expression that describes the aspect ratio of wrinkles as a function of both applied load and roller radius.

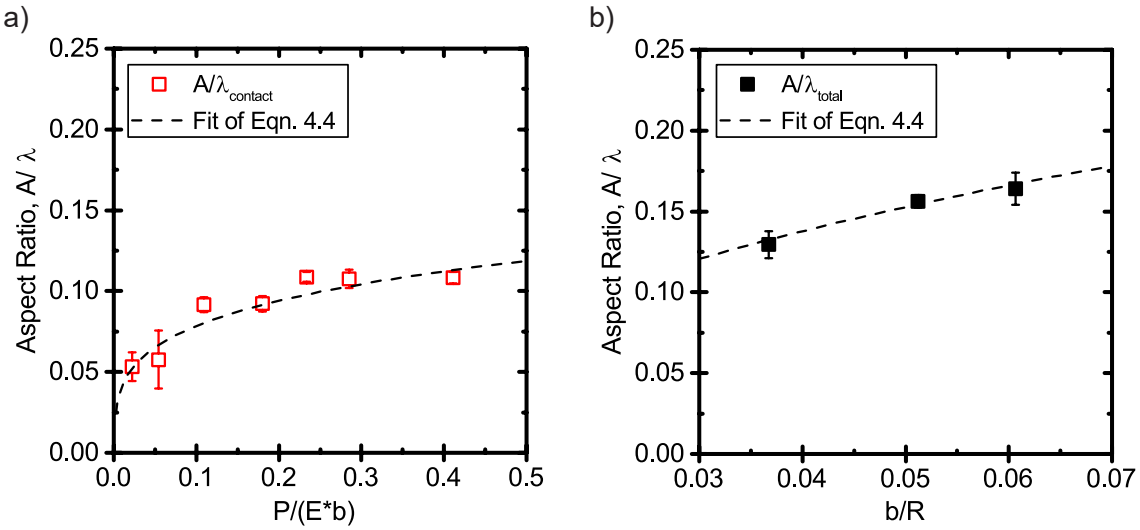

Figure 4.7. Wrinkle aspect ratio influenced by applied load and roller radius. a) The aspect ratio of wrinkles created from contact deformation was quantified from amplitude and wavelength values measured using optical profilometry (open red squares). Aspect ratio for the FEM was calculated with Equation 4.3 using materials properties and geometry values from wrinkling experiments (open blue circles). Equation 4.4 (dashed line) is fit to the data by the critical strain for wrinkling, ε_c. b) The influence of roller radius on the aspect ratio of wrinkles created from both $\varepsilon_{contact}$ and $\varepsilon_{bending}$ is plotted (solid black squares). Equation 4.4 (dashed line) is fit to the data by the critical strain for wrinkling, ε_c. Figure reproduced with permission from Ref [125].

$$\left(\frac{A}{\lambda}\right)_{total} = \frac{2t}{\lambda}\left\{\frac{1}{\varepsilon_c}\left[C_1\left(\frac{P}{\overline{E}_s\, b}\right)^{0.49}\left(\frac{b}{R}\right)^{0.74} + C_2\left(\frac{b}{R}\right)\right] - 1\right\}^{1/2} \tag{4.4}$$

Using our process constants of b and $\overline{E}_s$, as well as fitted values of n, m, C_1, and C_2, we plot Equation 4.4 for our applied load data (Figure 4.7a) and for our roller radius data (Figure 4.7b) while fitting the critical strain for wrinkling, ε_c. For the case of applied load, we find good agreement between Equation 4.4 and the experimental data, where $\varepsilon_c = .0011$. For the case of roller radius, we also find good agreement between Equation 4.4 and the experimental data, where $\varepsilon_c = .0009$. These values are in agreement with our predicted ε_c value of 0.0010, calculated from Equation 1.10. To determine a critical load for wrinkling during the rolling process we input the fitted ε_c value into Equation 4.1 and rearrange.

$$P_c = \left[\frac{\varepsilon_c}{C_1}\left(\frac{R}{b}\right)^m\right]^{1/n} \overline{E}_s \; b \tag{4.5}$$

From this equation, we find that the load required to induce wrinkling during the rolling process is 0.32 N/m. If, during the laminating process, applied load is actuated above and below this critical load, wrinkling can be switched on and off, leading to interesting surface architectures.

4.6 Conclusions

These experiments demonstrate a repeatable, versatile process using the mechanics of existing manufacturing techniques, including film lamination and transfer coating, to create wrinkled surfaces. The semi-empirical equations demonstrate understanding of the important contributions to the mechanism of contact deformation and bending on wrinkle creation. Based on these findings, we understand the specific relationships between wrinkle dimensions and the process parameters, including P, $\overline{E}_s$, R, and b. With these predictions, a scalable process to create surface wrinkles is easily envisioned.

4.7 Acknowldgements

M. Imburgia would like to thank Y. Ebata, H.-S. Kim, M. Reyes-Martinez, and Y.-C. Chen for their insight and help with experiments and Y.-C. Chen and H. Meeran for their help with editing this document. The authors would like to thank the Human Frontiers Science Program (RPG0034/2012) for funding.

CHAPTER 5

SUMMARY AND OUTLOOK

Throughout this dissertation, we studied soft material deformation and adhesion for systems with application to bio-inspired adhesives and wrinkled surface fabrication. The presence of van der Waals forces between a soft adhesive and a rigid contacting surface was the dominant molecular mechanism of adhesion for all three studies. Understanding the deformation of the soft adhesive layer and how the system loading and geometry influences non-linear mechanical transitions, including interfacial failure and surface buckling, are crucial for predicting the performance of the mechanical system.

5.1 Reversible adhesive system with multiple contacts

5.1.1 Summary

In Chapter 2 we studied the deformation and adhesion of a multi-component fabric-elastomer system with multiple adhesive contacts, called "digits". Direct relations between compliance of the loading system and adhesive digit compliance, contact area, and angular spacing were developed using lap adhesion experiments. Additionally, a scaling of adhesive force capacity in a multi-component system as a function of angular spacing between digits was derived.

5.1.2 Outlook

This specific geometric arrangement of adhesive digits has several implications for the study and design of reversible adhesive systems. First, active control of adhesive

force for a synthetic device with multiple contact surfaces can be achieved by controlling angular spacing of adhesive digits. Second, the framework set by the equations shown here can lead to more complex device design of adhesive components with varying compliance.

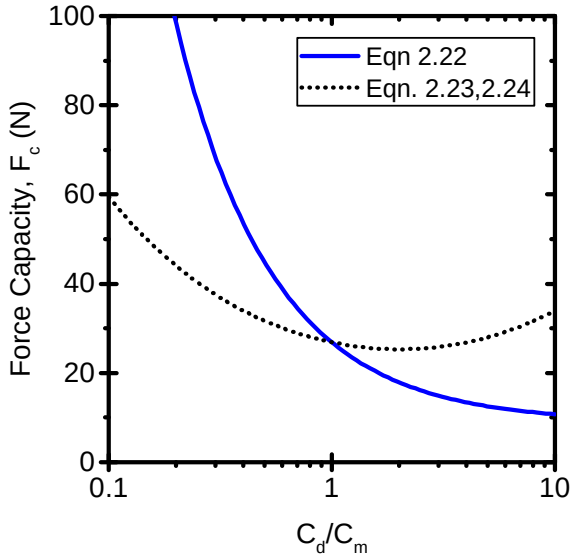

Figure 5.1. Compliance variation on adhesive force capacity. Force capacity versus digit compliance ratio, C_d/C_m, is represented in the plot for $\theta = 0$. Using values of adhesive area, G_c, and middle digit compliance, C_m, from our experiments, the various force capacity criteria in a three-digit system for $\theta = 0$ as a function of outer digit compliance, C_d, is plotted. The force capacity criterion of Equation 2.22 using the given input parameters is represented by the solid blue line. The dotted black line represents the force capacity criteria of Equations 2.23 and 2.24

As an example, our developed relations quantitatively describe variation in adhesive force for existing studies that involve the loading of multiple adhesive contacts simultaneously. To highlight this comparison, we present Figure 5.1, which represents a variation in the compliance of the outer two digits, C_d, relative to the compliance of the middle digit, C_m, and the impact on overall force capacity. Using values of adhesive area, G_c, and middle digit compliance, C_m, from our experiments, the various force capacity criteria in a three-digit system for $\theta = 0$ as a function of outer digit compliance variation, C_d, are plotted. For values of $C_d/C_m > 1$, the outer digits

are more compliant than the middle digit. Using Equations 2.22-2.24 we predict the middle digit will fail first, leading to Equation 2.22 as the adhesive system design criterion for $C_d/C_m > 1$. For the case where $C_d/C_m < 1$, the outer digits are less compliant than the middle digits. Using Equations 2.22-2.24 we predict that the outer digits will fail first, leading to either Equation 2.23 or 2.24 as the adhesive system design criteria for $C_d/C_m < 1$. This demonstration highlights how the variability in compliances of individual digits can predict the variability in adhesive force capacity of a multiple adhesive contact system using Equations 2.22-2.24 and various measured input parameters of digit geometry and materials properties.

Finally, these equations serve as a foundation for studying the biomechanics of animals that use adhesion for locomotion, particularly for addressing the influence of adhesive toe configuration on the variation in adhesive force capacity.

5.2 Compliance of an isolated shear contact

5.2.1 Summary

In Chapter 3 we examined the deformation and adhesion of a rigid punch contacting and shearing a thin elastic coating. We found that the shear compliance of the coating is non-linearly and inversely dependent on the confinement ratio, or ratio of contact radius, a, to coating thickness, h (a/h). Finite-element analysis was performed to support experiments, leading to the development of an explicit, semi-empirical relation between shear compliance and confinement ratio. We also developed a relation between adhesive force capacity and confinement ratio, finding that an increase in adhesive force capacity was largely dictated by an increase in confinement, with some additional contributions attributed to dissipative processes confined to the adhesive crack tip.

5.2.2 Outlook

The loading system and geometry presented here are present in many applications ranging from rubber tire friction to bio-inspired adhesion. We expect the compliance equation will serve as a guide for decoupling geometry and materials parameters for explaining the scaling of compliance involving a thin elastic layer. Our treatment of the adhesive force capacity for reversible adhesive systems involving a thin elastic layer agrees well with experimental findings, but several caveats require mention.

The relation of adhesive force capacity with compliance assumes the instantaneous and catastrophic propagation of an interfacial crack as soon as the adhesive failure criterion is met. Experimentally, we do not observe catastrophic failure, but steady crack propagation. The steady crack propagation is most likely due to different dissipative processes confined to the adhesive crack tip. This discrepancy between assumptions and experimental evidence is captured by the fitting parameter, G_c, and does not devalue the finding that compliance is a dominant factor in determining adhesive force capacity in our system. However, further experiments can be conducted, such as chemically functionalizing adhesive surfaces, to reduce rate dependent adhesion and increase the probability for catastrophic adhesive failure. Additionally, some of the experimental conditions in our shear loading experiments caused a pronounced peel moment, the result of a limitation of the experimental setup. By redesigning the experimental setup to more precisely reduce the distance between force application and the adhesive surface, ℓ, the peel moment can be reduced. This redesign would also allow for access to small probe diameters and thinner elastic coatings, widening the appeal of our force and compliance relations to applications in the micrometer range, such as micro-transfer printing and microelectronics.

5.3 Rolling wrinkles on elastic substrates

5.3.1 Summary

In Chapter 4 we developed a fabrication technique that transforms the existing manufacturing process of film lamination to create tunable wrinkled surfaces in a thin film/soft elastomer composite. We tuned the size of wrinkles by controlling the amount of tensile strain in the soft elastomer layer before lamination of the thin film. Tensile strain in the elastomer was controlled by rolling contact deformation and bending of an initially flat elastomer around a curved roller. Finite-element modeling was conducted to develop a semi-empirical relation describing the influence of applied load on tensile strain during rolling contact. Using these experiments and analyses, we developed a relation between wrinkle aspect ratio and the process parameters of applied contact load and roller curvature to highlight the direct influence of tunable parameters in this film lamination process.

5.3.2 Outlook

Wrinkled surface technology has been envisioned in many applications ranging from optoelectronics to enhanced adhesives. The technique presented here to tune wrinkle size in a continuous process can lead to the large scale manufacturing of previously proposed wrinkling technologies.

Additionally, our materials system can be expanded to incorporate inorganic films, as demonstrated in Figure 5.2. During the film lamination and wrinkling process humidity is introduced to the system to weaken the interface between the polymer film and the silicon substrate. However, for inorganic films, of which surface energies are typically significantly higher than organic films, humidity proves insufficient to aid in film transfer from a support substrate to poly(dimethylsiloxane) [PDMS] layer. As a proof of concept we successfully laminated a gold film onto a PDMS substrate using a sacrificial polymer layer, the details of which are listed below.

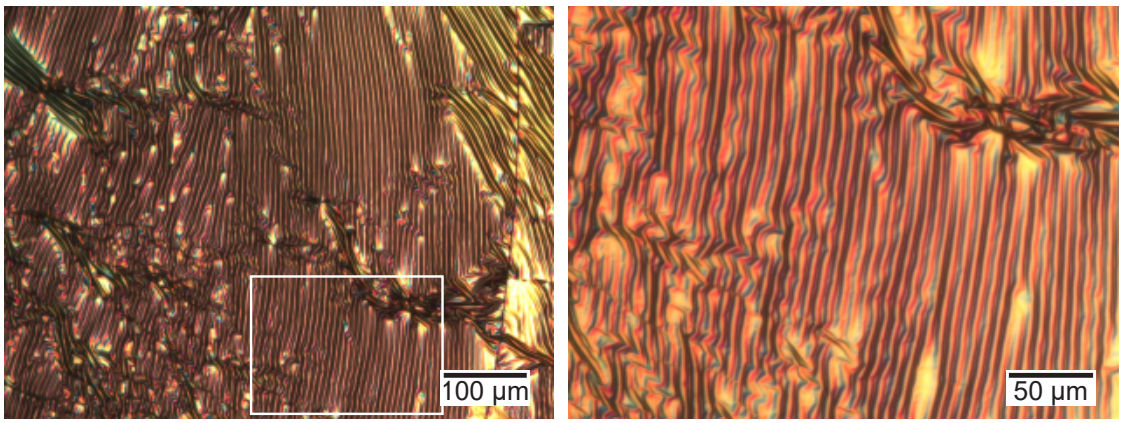

Figure 5.2. Wrinkled gold film. Left: Optical micrograph of a 50nm gold film transfered and wrinkled onto a 2mm PDMS substrate using the rolling wrinkles technique. White rectangle represents the location of the right image. Right: expanded image of the wrinkled gold film.

To prepare the gold film a 20nm water-soluble poly(acrylic acid) [PAA] film is first spun-coat from 1.5wt% water solution onto a cleaned silicon wafer. Next, a 50nm film of gold is evaporated onto the PAA using chemical vapor deposition. The gold film is then laminated and wrinkled on a support PDMS layer using our film lamination and wrinkling technique. During this process humidity is introduced to the system to weaken the adhesion between the PAA layer and silicon substrate, allowing for preferential transfer of the gold onto the PDMS. This example supports the ability to expand materials systems into inorganic films, laying a foundation for surface wrinkling applications ranging from thin-film transistor arrays to stretchable photovoltaics.

5.4 Funding sources

The work in this dissertation was generously supported by several funding agencies including the Human Frontiers Science Program (RPG0034/2012), the National Science Foundation MRSEC at UMass, and UMass Life Science Moment Fund.

BIBLIOGRAPHY

[1] Shepherd, R. F.; Ilievski, F.; Choi, W.; Morin, S. A.; Stokes, A. A.; Mazzeo, A. D.; Chen, X.; Wang, M.; Whitesides, G. M. *Proceedings of the National Academy of Sciences of the United States of America* **2011**, *108*, 20400–20403.

[2] Brown, E.; Rodenberg, N.; Amend, J.; Mozeika, A.; Steltz, E.; Zakin, M. R.; Lipson, H.; Jaeger, H. M. *Proceedings of the National Academy of Sciences* **2010**, *107*, 18809–18814.

[3] Robinson, S. S.; O'Brien, K. W.; Zhao, H.; Peele, B. N.; Larson, C. M.; Mac Murray, B. C.; van Meerbeek, I. M.; Dunham, S. N.; Shepherd, R. F. *Extreme Mechanics Letters* **2015**, *5*, 47–53.

[4] Mironov, V.; Boland, T.; Trusk, T.; Forgacs, G.; Markwald, R. R. *Trends in Biotechnology* **2003**, *21*, 157–161.

[5] Lee, W.; Lee, V.; Polio, S.; Keegan, P.; Lee, J.-H.; Fischer, K.; Park, J.-K.; Yoo, S.-S. *Biotechnology and Bioengineering* **2010**, *105*, n/a–n/a.

[6] Kolesky, D. B.; Truby, R. L.; Gladman, A. S.; Busbee, T. A.; Homan, K. A.; Lewis, J. A. *Advanced Materials* **2014**, *26*, 3124–3130.

[7] Creton, C.; Gorb, S. N. *MRS Bulletin* **2007**, *32*, 466–472.

[8] Jagota, A.; Hui, C.-Y. *Materials Science and Engineering: R: Reports* **2011**, *72*, 253–292.

[9] Bartlett, M. D.; Croll, A. B.; King, D. R.; Paret, B. M.; Irschick, D. J.; Crosby, A. J. *Advanced Materials* **2012**, *24*, 1078–1083.

[10] Rogers, J. A.; Someya, T.; Huang, Y. Y. *Science* **2010**, *327*, 1603–7.

[11] Majidi, C.; Kramer, R.; Wood, R. J. *Smart Materials and Structures* **2011**, *20*, 105017.

[12] Bartlett, M. D.; Fassler, A.; Kazem, N.; Markvicka, E. J.; Mandal, P.; Majidi, C. *Advanced Materials* **2016**, n/a–n/a.

[13] Gent, A. N. Rubber and rubber elasticity: a review. Journal of Polymer Science: Polymer Symposia. 1974; pp 1–17.

[14] Israelachvili, J. N.; Tabor, D. *Proceedings of the Royal Society A: Mathematical, Physical and Engineering Sciences* **1972**, *331*, 19–38.

[15] Griffith, A. A. *Philosophical Transactions of the Royal Society A: Mathematical, Physical and Engineering Sciences* **1921**, *221*, 163–198.

[16] Shull, K. R. *Materials Science and Engineering R: Reports* **2002**, *36*, 1–45.

[17] Shull, K. R.; Ahn, D.; Chen, W.-L.; Flanigan, C. M.; Crosby, A. J. *Macromolecular Chemistry and Physics* **1998**, *199*, 485–511.

[18] Arzt, E.; Gorb, S. N.; Spolenak, R. *Proceedings of the National Academy of Sciences of the United States of America* **2003**, *100*, 10603–6.

[19] Federle, W.; Barnes, W. J. P.; Baumgartner, W.; Drechsler, P.; Smith, J. M. *Journal of the Royal Society, Interface / the Royal Society* **2006**, *3*, 689–697.

[20] Bullock, J. M. R.; Drechsler, P.; Federle, W. *The Journal of experimental biology* **2008**, *211*, 3333–43.

[21] Labonte, D.; Federle, W. *Philosophical transactions of the Royal Society of London. Series B, Biological sciences* **2015**, *370*, 20140027.

[22] Autumn, K.; Sitti, M.; Liang, Y. A.; Peattie, A. M.; Hansen, W. R.; Sponberg, S.; Kenny, T. W.; Fearing, R.; Israelachvili, J. N.; Full, R. J. *Proceedings of the National Academy of Sciences of the United States of America* **2002**, *99*, 12252–6.

[23] Hawkes, E. W.; Eason, E. V.; Christensen, D. L.; Cutkosky, M. R. *Journal of the Royal Society, Interface / the Royal Society* **2015**, *12*, 20140675.

[24] King, D. R.; Bartlett, M. D.; Gilman, C. A.; Irschick, D. J.; Crosby, A. J. *Advanced Materials* **2014**, *26*, 4345–4351.

[25] Gilman, C. A.; Imburgia, M. J.; Bartlett, M. D.; King, D. R.; Crosby, A. J.; Irschick, D. J. *PloS ONE* **2015**, *10*, 1–15.

[26] Russell, A. *Canadian Journal of Zoology* **1986**, *64*, 948–955.

[27] Bowden, N.; Huck, W. T. S.; Paul, K. E.; Whitesides, G. M. *Applied Physics Letters* **1999**, *75*, 2557.

[28] Cerda, E.; Mahadevan, L. *Physical Review Letters* **2003**, *90*, 1–4.

[29] Chen, X.; Hutchinson, J. W. *Journal of Applied Mechanics* **2004**, *71*, 597.

[30] Huang, Z.; Hong, W.; Suo, Z. *Journal of the Mechanics and Physics of Solids* **2005**, *53*, 2101–2118.

[31] Breid, D.; Crosby, A. J. *Soft Matter* **2011**, *7*, 4490–4496.

[32] Pocivavsek, L.; Dellsy, R.; Kern, A.; Johnson, S.; Lin, B.; Lee, K. Y. C.; Cerda, E. *Science* **2008**, *320*, 912–6.

[33] Ebata, Y.; Croll, A. B.; Crosby, A. J. *Soft Matter* **2012**, *8*, 9086–9091.

[34] Zang, J.; Zhao, X.; Cao, Y.; Hutchinson, J. W. *Journal of the Mechanics and Physics of Solids* **2012**, *60*, 1265–1279.

[35] Chen, Y.-C.; Crosby, A. J. *Advanced Materials* **2014**, *26*, 5626–31.

[36] Wang, Q.; Zhao, X. *Scientific Reports* **2015**, *5*, 8887.

[37] Genzer, J.; Groenewold, J. *Soft Matter* **2006**, *2*, 310–323.

[38] Biot, M. *Journal of Applied Mechanics* **1937**, *4*, 1–7.

[39] Holten-Andersen, N.; Harrington, M. J.; Birkedal, H.; Lee, B. P.; Messersmith, P. B.; Lee, K. Y. C.; Waite, J. H. *Proceedings of the National Academy of Sciences of the United States of America* **2011**, *108*, 2651–2655.

[40] Autumn, K.; Liang, Y. A.; Hsieh, S. T.; Zesch, W.; Chan, W. P.; Kenny, T. W.; Fearing, R.; Full, R. J. *Nature* **2000**, *405*, 681–5.

[41] Barquins, M. *Journal of Applied Polymer Science* **1983**, *28*, 2647–2657.

[42] Bartlett, M. D.; Croll, A. B.; Crosby, A. J. *Advanced Functional Materials* **2012**, *22*, 4985–4992.

[43] Bartlett, M. D.; Crosby, A. J. *Advanced Materials* **2014**, *26*, 3405–3409.

[44] King, D. R.; Crosby, A. J. *ACS Applied Materials & Interfaces* **2015**, *7*, 27771–27781, PMID: 26618537.

[45] Risan, J.; Croll, A. B.; Azarmi, F. *Journal of Polymer Science Part B: Polymer Physics* **2015**, *53*, 48–57.

[46] Wang, Z.; Dai, Z.; Ji, A.; Ren, L.; Xing, Q.; Dai, L. *Bioinspiration & Biomimetics* **2015**, *10*, 016019.

[47] Autumn, K.; Hsieh, S. T.; Dudek, D. M.; Chen, J.; Chitaphan, C.; Full, R. J. *The Journal of experimental biology* **2006**, *209*, 260–272.

[48] Birn-Jeffery, A. V.; Higham, T. E. *Biology letters* **2014**, *10*, 20140456.

[49] Birn-Jeffery, A. V.; Higham, T. E. *Frontiers in Zoology* **2016**, *13*, 11.

[50] Kuo, C.-Y.; Briggs, D. R.; Irschick, D. J. *unpublished data* **2016**,

[51] Behera, B. K.; Hari, P. *Woven textile structure: Theory and applications*; Elsevier, 2010.

[52] Kaelble, D. H. *Journal of Rheology* **1960**, *4*, 45.

[53] Newby, B.-m. Z.; Chaudhury, M. K. *Langmuir* **1998**, *7463*, 4865–4872.

[54] Maugis, D.; Barquins, M. *Journal of Physics D: Applied Physics* **1978**, *11*, 1989–2023.

[55] Del Campo, A.; Greiner, C.; Arzt, E. *Langmuir* **2007**, *23*, 10235–10243.

[56] Crosby, A. J.; Hageman, M.; Duncan, A. *Langmuir* **2005**, *21*, 11738–43.

[57] Qu, L.; Dai, L.; Stone, M.; Xia, Z.; Wang, Z. L. *Science (New York, N.Y.)* **2008**, *322*, 238–242.

[58] Webster, N. B.; Johnson, M. K.; Russell, A. P. *Acta Zoologica* **2009**, *90*, 18–29.

[59] Peattie, A. M.; Full, R. J. *Proceedings of the National Academy of Sciences of the United States of America* **2007**, *104*, 18595–18600.

[60] Irschick, D. J.; Austin, C. C.; Petren, K.; Fisher, R. N.; Losos, J. B.; Ellers, O. *Biological Journal of the Linnean Society* **1996**, *59*, 21–35.

[61] Mindlin, R. D. *Journal of Applied Mechanics* **1949**, *16*, 259–268.

[62] Savkoor, R.; Briggs, G. *Proceedings of the Royal Society A: Mathematical, Physical and Engineering Sciences* **1977**, *356*, 103–114.

[63] Hay, J.; Pharr, G. *ASM Handbook Volume 08: Mechanical Testing and Evaluation*; 2000; pp 231–242.

[64] Johnson, K.; Kendall, K.; Roberts, A. D. *Proceedings of the Royal Society of London. Series A, Mathematical and Physical Sciences* **1971**, *324*, 301–313.

[65] Barquins, M.; Maugis, D. *Journal of Adhesion* **1981**, *13*, 53–65.

[66] Basire, C.; Fretigny, C. *EPJ E, AppliedPhysics* **1999**, *6*, 323–329.

[67] Schallamach, A. *Wear* **1971**, *17*, 301–312.

[68] Chaudhury, M. K.; Chung, J. Y. *Langmuir* **2007**, *23*, 8061–8066.

[69] Shen, L.; Glassmaker, N. J.; Jagota, A.; Hui, C.-Y. *Soft Matter* **2008**, *4*, 618.

[70] Bartlett, M. D.; Crosby, A. J. *Materials Horizons* **2014**, *1*, 507–512.

[71] Cua, A.; Wilhelm, K.-P.; Maibach, H. *British Journal of Dermatology* **1990**, *123*, 473–479.

[72] Ganghoffer, J.-F.; Gent, A. N. *Journal of Adhesion* **1995**, *48*, 75–84.

[73] Creton, C.; Lakrout, H. *Journal of Polymer Science Part B: Polymer Physics* **2000**, *38*, 965–979.

[74] Bartlett, M. D.; Crosby, A. J. *Langmuir* **2013**, *29*, 11022–7.

[75] Barquins, M.; Koudine, A.; Vallet, D. *Comptes rendus de l'Académie des sciences* **1996**, *323*, 433–438.

[76] Rand, C. J.; Crosby, A. J. *Applied Physics Letters* **2007**, *91*, 261909.

[77] Chaudhury, M. K.; Kim, K. *European Physical Journal E* **2007**, *23*, 175–83.

[78] Timoshenko, S. P.; Goodier, J. N. *Theory of Elasticity*, 2nd ed.; McGraw-Hill: New York, 1951.

[79] Shull, K. R.; Flanigan, C. M.; Crosby, A. J. *Physical Review Letters* **2000**, *84*, 3057–60.

[80] Rand, C. J.; Crosby, A. J. *Applied Physics Letters* **2006**, *89*, 261907.

[81] Harrison, C.; Stafford, C. M.; Zhang, W.; Karim, A. *Applied Physics Letters* **2004**, *85*, 4016–4018.

[82] Yoo, P. J. *Electronic Materials Letters* **2011**, *7*, 17–23.

[83] Koo, W. H.; Jeong, S. M.; Araoka, F.; Ishikawa, K.; Nishimura, S.; Toyooka, T.; Takezoe, H. *Nature Photonics* **2010**, *4*, 222–226.

[84] Oh, S. J.; Kagan, C. R.; Kim, J. B.; Kim, P.; Pe, N. C.; Fleischer, J. W.; Stone, H. A.; Loo, Y.-l. *Nature photonics* **2012**, *6*, 327–332.

[85] Watanabe, M.; Shirai, H.; Hirai, T. *Journal of Applied Physics* **2002**, *92*, 4631–4637.

[86] Lacour, S. P.; Wagner, S.; Huang, Z.; Suo, Z. *Applied Physics Letters* **2003**, *82*, 2404–2406.

[87] Wagner, S.; Lacour, S. P.; Jones, J.; Hsu, P. H. I.; Sturm, J. C.; Li, T.; Suo, Z. *Physica E: Low-Dimensional Systems and Nanostructures* **2004**, *25*, 326–334.

[88] Khang, D.-Y.; Jiang, H.; Huang, Y.; Rogers, J. A. *Science* **2006**, *311*, 208–12.

[89] Kim, D.-H.; Ahn, J.-H.; Choi, W. M.; Kim, H.-S.; Kim, T.-H.; Song, J.; Huang, Y. Y.; Liu, Z.; Lu, C.; Rogers, J. A. *Science* **2008**, 507–511.

[90] Reyes-Martinez, M. A.; Crosby, A. J.; Briseno, A. L. *Nature Communications* **2015**, *6*, 6948.

[91] Chan, E. P.; Crosby, A. J. *Advanced Materials* **2006**, *18*, 3238–3242.

[92] Chandra, D.; Yang, S.; Lin, P. C. *Applied Physics Letters* **2007**, *91*, 89–92.

[93] Kim, H. S.; Crosby, A. J. *Advanced Materials* **2011**, *23*, 4188–4192.

[94] Chan, E. P.; Smith, E. J.; Hayward, R. C.; Crosby, A. J. *Advanced Materials* **2008**, *20*, 711–716.

[95] Lin, P.-C.; Vajpayee, S.; Jagota, A.; Hui, C.-Y.; Yang, S. *Soft Matter* **2008**, *4*, 1830–1835.

[96] Rand, C. J.; Crosby, A. J. *Journal of Applied Physics* **2009**, *106*, 064913.

[97] Davis, C. S.; Crosby, A. J. *Soft Matter* **2011**, *7*, 5373.

[98] Vajpayee, S.; Khare, K.; Yang, S.; Hui, C.-Y.; Jagota, A. *Advanced Functional Materials* **2011**, *21*, 547–555.

[99] Chung, J. Y.; Youngblood, J. P.; Stafford, C. M. *Soft Matter* **2007**, *3*, 1163.

[100] Lin, P.-C.; Yang, S. *Soft Matter* **2009**, *5*, 1011.

[101] Khare, K.; Zhou, J.; Yang, S. *Langmuir* **2009**, *25*, 12794–12799.

[102] Efimenko, K.; Finlay, J.; Callow, M. E.; Callow, J. A.; Genzer, J. *ACS Applied Materials and Interfaces* **2009**, *1*, 1031–1040.

[103] Ohzono, T.; Monobe, H. *Langmuir* **2010**, *26*, 6127–6132.

[104] Mei, Y.; Thurmer, D. J.; Cavallo, F.; Kiravittaya, S.; Schmidt, O. G. *Advanced Materials* **2007**, *19*, 2124–2128.

[105] Chung, S.; Lee, J. H.; Moon, M. W.; Han, J.; Kamm, R. D. *Advanced Materials* **2008**, *20*, 3011–3016.

[106] Ohzono, T.; Monobe, H.; Shiokawa, K.; Fujiwara, M.; Shimizu, Y. *Soft Matter* **2009**, *5*, 4658.

[107] Efimenko, K.; Rackaitis, M.; Manias, E.; Vaziri, A.; Mahadevan, L.; Genzer, J. *Nature materials* **2005**, *4*, 293–297.

[108] Lu, N.; Yoon, J.; Suo, Z. *International Journal of Materials Research* **2007**, *98*, 717–722.

[109] Jiang, X.; Takayama, S.; Qian, X.; Ostuni, E.; Wu, H.; Bowden, N.; LeDuc, P.; Ingber, D. E.; Whitesides, G. M. *Langmuir* **2002**, *18*, 3273–3280.

[110] Lam, M. T.; Sim, S.; Zhu, X.; Takayama, S. *Biomaterials* **2006**, *27*, 4340–4347.

[111] Zimberlin, J. A.; Wadsworth, P.; Crosby, A. J. *Cell motility and the cytoskeleton* **2008**, *65*, 762–7.

[112] Vandeparre, H.; Gabriele, S.; Brau, F.; Gay, C.; Parker, K. K.; Damman, P. *Soft Matter* **2010**, *6*, 5751.

[113] Guvendiren, M.; Burdick, J. A. *Biomaterials* **2010**, *31*, 6511–6518.

[114] Guvendiren, M.; Burdick, J. A. *Advanced Healthcare Materials* **2013**, *2*, 155–164.

[115] Stafford, C. M.; Harrison, C.; Beers, K. L.; Karim, A.; Amis, E. J.; VanLandingham, M. R.; Kim, H.-C.; Volksen, W.; Miller, R. D.; Simonyi, E. E. *Nature materials* **2004**, *3*, 545–550.

[116] Stafford, C. M.; Vogt, B. D.; Harrison, C.; Julthongpiput, D.; Huang, R. *Macromolecules* **2006**, *39*, 5095–5099.

[117] Wilder, E. A.; Guo, S.; Lin-Gibson, S.; Fasolka, M. J.; Stafford, C. M. *Macromolecules* **2006**, *39*, 4138–4143.

[118] Tank, D.; Lee, H. H.; Khang, D.-Y. *Macromolecules* **2009**, *42*, 7079–7083.

[119] O'Connor, B.; Chan, E. P.; Chan, C.; Conrad, B. R.; Richter, L. J.; Kline, R. J.; Heeney, M.; McCulloch, I.; Soles, C. L.; DeLongchamp, D. M. *ACS Nano* **2010**, *4*, 7538–44.

[120] Chan, E. P.; Kundu, S.; Lin, Q.; Stafford, C. M. *ACS Applied Materials and Interfaces* **2011**, *3*, 331–8.

[121] Reyes-Martinez, M. A.; Ramasubramaniam, A.; Briseno, A. L.; Crosby, A. J. *Advanced Materials* **2012**, *24*, 5548–5552.

[122] Sharma, B. K.; Jang, B.; Lee, J. E.; Bae, S.-H.; Kim, T. W.; Lee, H.-J.; Kim, J.-H.; Ahn, J.-H. *Advanced Functional Materials* **2012**, *23*, 2024–2032.

[123] Kim, J. Y.; Choi, H.-J.; Woo, C.-S. *International Journal of Precision Engineering and Manufacturing* **2014**, *15*, 711–716.

[124] Guo, Q.; Zhang, M.; Xue, Z.; Ye, L.; Wang, G.; Huang, G.; Mei, Y.; Wang, X.; Di, Z. *Applied Physics Letters* **2013**, *103*, 264102.

[125] Imburgia, M. J.; Crosby, A. J. *Extreme Mechanics Letters* **2016**, *6*, 23–30.

[126] Bentall, R.; Johnson, K. *International Journal of Mechanical Sciences* **1968**, *10*, 637–663.

[127] Deshpande, N. *TAPPI Journal* **1978**, *61*, 115–118.

[128] Soong, T.-C.; Li, C. *International Journal of Mechanical Sciences* **1981**, *23*, 263–273.

[129] Soong, T.-C.; Li, C. *Journal of Applied Mechanics* **1981**, *48*, 889–894.

[130] Good, J.; Wu, Z. *Journal of Applied Mechanics* **1993**, *60*, 942–947.

[131] Reynolds, O. *Philosophical Transactions of the Royal Society of London* **1876**, *166*, 155–174.

[132] Johnson, K. *Contact Mechanics*, 1st ed.; Cambridge University Press: Cambridge, 1985.

[133] Pu, Z. In *Polymer Data Handbook*, 2nd ed.; Mark, J. E., Ed.; 2009; pp 1031–1038.